NUREG/CR-6638
ANL-99/9

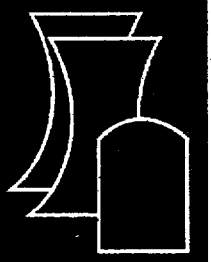

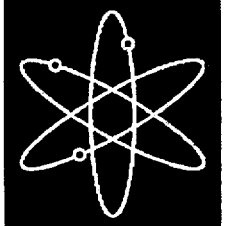

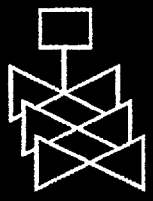

Advanced NDE for Steam Generator Tubing

Argonne National Laboratory

U.S. Nuclear Regulatory Commission
Office of Nuclear Regulatory Research
Washington, DC 20555-0001

AVAILABILITY NOTICE

Availability of Reference Materials Cited in NRC Publications

NRC publications in the NUREG series, NRC regulations, and *Title 10, Energy,* of the *Code of Federal Regulations,* may be purchased from one of the following sources:

1. The Superintendent of Documents
   U.S. Government Printing Office
   P.O. Box 37082
   Washington, DC 20402–9328
   <http://www.access.gpo.gov/su_docs>
   202–512–1800
2. The National Technical Information Service
   Springfield, VA 22161–0002
   <http://www.ntis.gov>
   1–800–553–6847 or locally 703–605–6000

The NUREG series comprises (1) brochures (NUREG/BR-XXXX), (2) proceedings of conferences (NUREG/CP-XXXX), (3) reports resulting from international agreements (NUREG/IA-XXXX), (4) technical and administrative reports and books [(NUREG-XXXX) or (NUREG/CR-XXXX)], and (5) compilations of legal decisions and orders of the Commission and Atomic and Safety Licensing Boards and of Office Directors' decisions under Section 2.206 of NRC's regulations (NUREG-XXXX).

A single copy of each NRC draft report for comment is available free, to the extent of supply, upon written request as follows:

Address: Office of the Chief Information Officer
Reproduction and Distribution
Services Section
U.S. Nuclear Regulatory Commission
Washington, DC 20555–0001
E–mail: <DISTRIBUTION@nrc.gov>
Facsimile: 301–415–2289

A portion of NRC regulatory and technical information is available at NRC's World Wide Web site:

<http://www.nrc.gov>

After January 1, 2000, the public may electronically access NUREG-series publications and other NRC records in NRC's Agencywide Document Access and Management System (ADAMS), through the Public Electronic Reading Room (PERR), link <http://www.nrc.gov/NRC/ADAMS/index.html>.

Publicly released documents include, to name a few, NUREG-series reports; *Federal Register* notices; applicant, licensee, and vendor documents and correspondence; NRC correspondence and internal memoranda; bulletins and information notices; inspection and investigation reports; licensee event reports; and Commission papers and their attachments.

Documents available from public and special technical libraries include all open literature items, such as books, journal articles, and transactions, *Federal Register* notices, Federal and State legislation, and congressional reports. Such documents as theses, dissertations, foreign reports and translations, and non-NRC conference proceedings may be purchased from their sponsoring organization.

Copies of industry codes and standards used in a substantive manner in the NRC regulatory process are maintained at the NRC Library, Two White Flint North, 11545 Rockville Pike, Rockville, MD 20852–2738. These standards are available in the library for reference use by the public. Codes and standards are usually copyrighted and may be purchased from the originating organization or, if they are American National Standards, from—

American National Standards Institute
11 West 42nd Street
New York, NY 10036–8002
<http://www.ansi.org>
212–642–4900

NUREG/CR-6638
ANL-99/9

Advanced NDE for Steam Generator Tubing

Manuscript Completed: October 1999
Date Published: January 2000

Prepared by
S. Bakhtiari, D. S. Kupperman

Argonne National Laboratory
9700 South Cass Avenue
Argonne, IL 60439

J. Muscara, NRC Project Manager

Prepared for
Division of Engineering Technology
Office of Nuclear Regulatory Research
U.S. Nuclear Regulatory Commission
Washington, DC 20555-0001
NRC Job Code W6487

NUREG/CR-6638 has been reproduced from the best available copy.

Advanced NDE for Steam Generator Tubing

S. Bakhtiari and D. S. Kupperman

Abstract

This report provides an assessment of various advanced nondestructive evaluation (NDE) techniques for inservice inspection of steam generator tubing. Selected results are presented on the application of data processing and visualization techniques; data analysis, including depth sizing and the development of correlations between eddy current signals and tube failure pressure by multivariate regression and neural networks; inspection of sleeved tubes; applications of ultrasonic NDE; and related work on emerging NDE technology.

Contents

Figures

Tables

Executive Summary

As part of a program on steam generator (SG) tube integrity sponsored by the U.S. Nuclear Regulatory Commission (USNRC) at Argonne National Laboratory, the reliability of nondestructive evaluation (NDE) methods for the detection and characterization of defects in SG tubing is being evaluated. In addition to work on the effectiveness of current NDE techniques, the potential impact of advanced and emerging inspection technology on the effectiveness of inspections is being assessed. This report provides an assessment of various advanced NDE techniques for the inservice inspection of SG tubing.

Multicoil rotating and array probe inspections generate enormous amounts of data. Conversion and manipulation codes have been developed to permit more efficient and flexible analysis of this data. Signal processing and data analysis algorithms have been developed that use the PC-based software MATLAB, which is a high-level scripting language that provides an efficient environment for the development of the algorithms as well as convenient graphical user interfaces (GUIs) and graphical displays of the results. A series of algorithms has been implemented under the MATLAB environment to carry out the conversion, normalization, and reformatting of eddy current (EC) readings for subsequent analysis. An interactive MATLAB program calls the data retrieval and calibration routines through a main GUI control window.

A flaw imaging and display software is described that attempts to simplify interpretation of data acquired by rotating and array probes through improved visualization and automated analysis methodologies. The software provides two views of the data: a two-dimensional plan view and a four-dimensional modified isometric view that uses color to represent relative phase information, unlike the conventional isometric plot, which presents only amplitude information. In its present form, the software estimates the depth of a flaw by using an algorithm similar to that used in conventional analysis. However, instead of estimating depth at isolated points that are selected by the analyst, it does so over the whole region around the flaw and presents the results in terms of a color map. This approach greatly improves "pattern recognition" and makes it much easier to see the morphology of the cracking and seems to reduce the dependence on the analyst's judgment. The 4–D modified isometric view has the advantage that it is relatively familiar to analysts accustomed to working with a conventional isometric plot, and also simultaneously provides relative phase information for every point in the region that surrounds the flaw.

Results are presented on the use of back-propagation neural-network structures to predict flaw depth. Our studies showed that, because accuracy is more critical for deep defects, the criteria for selecting training data could be weighted to include more samples with deeper defects and achieve an accuracy comparable to that obtained by using all of the available defects, with significantly shorter times required for training. Multivariate regression algorithms were evaluated as alternatives to neural-network structures for the development of correlations between EC data and flaw size.

Conventional repair and plugging criteria for SG tube integrity are based on estimated degradation depth. Tubes with EC indications that correspond to degradation greater than a specified limit (typically >40% of nominal tube wall thickness) are either repaired or plugged. For indications of outer-diameter stress corrosion cracking (ODSCC) at tube support plate (TSP)

locations, an alternate plugging criterion (APC) has been developed based on direct correlation of bobbin coil voltage amplitude (rather than estimated defect depth) to failure pressure and leak rate. The data on pulled and model boiler tube specimens that were originally used by the Westinghouse Owners Group to develop an APC for indications of ODSCC at TSP locations in Westinghouse plants with drilled tube support plates have been reanalyzed by multivariate regression analysis and neural network models. The global prediction bands of multivariate models are somewhat tighter than those achieved by a linear least–squares fit to the peak bobbin voltage. The linear models predict the failure pressures nearly as well as the nonlinear neural-network models.

The use of ultrasonic guided (Lamb) waves to improve detection of SG tubing flaws and to identify attributes that may be useful for characterizing defects in field-degraded tubes is also discussed. Because ultrasonic test (UT) methods involve shorter wavelengths, they inherently provide finer spatial resolution than EC methods; therefore, cracks that can be identified as segmented by ultrasonic interrogation, may only be resolvable as a single crack by EC examination. Studies have shown that the amplitude of Lamb wave echoes from flaws are not very sensitive to depth and hence provide little depth sizing information.

In collaboration with Sonoscan Inc. (Bensenville, IL), high-frequency ultrasonic imaging has been explored as a possible method to help characterize defects in SG tubes under laboratory conditions. Excellent results were obtained from laser-cut slots and from electro-discharge-machined (EDM) notches. However, SCCs, which are typically very tight, do not appear to produce shadows that are as clear as those produced by notches or fatigue cracks. Because the tip is the tightest portion of the crack, crack depths would be expected to be underestimated. The difficulties in estimating depths of SCCs by acoustic microscopy suggest that significant difficulties could also be encountered with procedures that attempt to use crack-tip echoes to estimate depth. Cracks that cannot be shadowed also will not scatter significant ultrasonic energy to reveal the location of the crack tip, resulting in underestimation of depth.

Acknowledgments

The authors acknowledge the contributions of D. R. Perkins and C. W. Vulyak to the experimental work described in this report. The authors thank M. Brook (ABB AMDATA), S. Canumalla (Sonoscan Inc.), C. V. Dodd, X. Kong (Northern Illinois University), and R. Kurtz (PNNL) for their contributions, and D. R. Diercks and W. J. Shack for their reviews and comments. This work is sponsored by the Office of Nuclear Regulatory Research, U.S. Nuclear Regulatory Commission (NRC), under FIN W6487; The NRC Project Manager is Dr. J. Muscara, who provided useful guidance in the performance of this work.

Acronyms and Abbreviations

ABB	ASEA Brown-Boveri
ANL	Argonne National Laboratory
APC	alternate plugging criterion
ARC	alternate repair criteria
ASME	American Society of Mechanical Engineers
ASTM	American Society for Testing and Materials
CSF	conjugate spectrum filters
EC	eddy current
EDM	electro-discharge-machined
EPRI	Electric Power Research Institute
FBH	flat-bottom hole
FIR	finite-impulse response
FTI	Framatome Technologies, Inc.
GUI	graphical user interface
HP	Hewlett Packard
ID	inner diameter
IDSCC	inner-diameter stress corrosion crack/cracking
IGA	intergranular attack
IIR	infinite-duration impulse response
IPC	interim plugging criterion
ISI	inservice inspection
LOOT	leave-one-out training
MLR	multiple linear regression
NDE	nondestructive evaluation
NRC	U.S. Nuclear Regulatory Commission
OD	outer diameter
ODSCC	outer-diameter stress corrosion crack/cracking
PC	(IBM) personal computer
PCR	principal component regression
PNNL	Pacific Northwest National Laboratory
RFEC	remote-field eddy current
RPC	rotating pancake coil
SCC	stress corrosion crack/cracking
SG	steam generator
S/N	signal-to-noise ratio
TOF	time of flight
TSP	tube support plate
TW	throughwall
UT	ultrasonic test/testing

1 Introduction

As part of a program on steam generator (SG) tube integrity sponsored by the U.S. Nuclear Regulatory Commission (USNRC) at Argonne National Laboratory (ANL), the reliability of nondestructive evaluation (NDE) methods for the detection and characterization of defects in SG tubing is being evaluated. In addition to work on the effectiveness of current NDE techniques, the potential impact of advanced and emerging inspection technology on the effectiveness of inspections is being assessed. In this report, an assessment of studies on advanced NDE techniques for the inservice inspection (ISI) of SG tubing. Results are presented on the application of data processing and visualization techniques; data analysis, including depth sizing and the development of correlations between eddy current (EC) signals and tube failure pressure by multivariate regression and neural networks; inspection of sleeved tubes; applications of ultrasonic NDE; and related work on emerging NDE technology.

2 Data Processing and Display

Multicoil rotating and array probe inspections generate enormous amounts of data. Conversion and manipulation codes have been developed to permit more efficient and flexible analysis of these data. The EC inspection system currently in use at ANL is a Zetec MIZ-30 EC inspection instrument under computer control by Eddynet95 software that runs on a HP workstation under the HP-UX operating system.

The NDE data acquired by this system is in a proprietary format that makes it difficult to process by algorithms other than those provided in the Eddynet95 environment. To facilitate development of improved algorithms for the evaluation of EC inspection results, codes have been developed to convert the raw inspection data to a standard ASCII file format.[1]

The data analysis and signal processing algorithms have been developed by using the PC-based software MATLAB, a high-level scripting language that provides an efficient environment for developing algorithms, as well as convenient graphical user interfaces (GUIs) and graphical displays of the results.

2.1 Computer-Aided EC Data Conversion and Calibration Routines

A series of algorithms has been implemented under the MATLAB environment to carry out the conversion, normalization, and reformatting of EC readings for subsequent analysis. An interactive MATLAB program, *ECTool*, calls the data retrieval and calibration routines through a single GUI control window. This software currently retrieves and processes inspection data acquired with either the Zetec MIZ-18 or MIZ-30 EC inspection instruments. With appropriate modifications, the software could also be used to retrieve inspection results from other standard commercial instruments.

The main control window contains virtual instrument controls such as pull-down menus, editable text, and push buttons that activate various functions for manipulation of the NDE results. Data files in standard Eddynet format are initially read by these codes. The data conversion routine extracts the essential header information (currently assumed to be from

MIZ-18 or MIZ-30 instruments), such as the number of channels and their associated frequencies, from the original Eddynet-formatted files. The decoded header information contains the frequency and channel configuration that is subsequently used to sort out raw EC readings. The reformatted data matrix, along with the header and coil configuration information, is then stored in a user-defined data file. Normalization values of all the available channels are calculated by using the inspection results from a calibration standard tube. These values consist of amplitude scaling factors, phase angle rotations, and null values that are automatically calculated based on user-defined approximate locations of known indications on the tube. Although the necessary information for standard normalization procedures is defined as a set of default values in the program, the code also allows calculation of these values in an arbitrary fashion. Finally, raw EC readings are calibrated by another code that is also activated from the main menu and applies the previously calculated normalization factors to each new raw data file. To avoid incorrect application of normalization factors, the codes initially check the header information for consistency between the original calibration standard tube and new data files that are subsequently loaded.

2.1.1 Conversion of Raw EC Inspection Results

Eddynet95 provides inspection data in MIZ-18 and MIZ-30 formats. The header sizes for MIZ-18 and MIZ-30 are currently preset to contain a fixed number of bytes. Following the header is the data stream with the sequence

horizontal	Channel 1	(2 byte signed integer)
vertical	Channel 1	(2 byte signed integer)
	...	
	...	
	...	
horizontal	Channel N	(2 byte signed integer)
vertical	Channel N	(2 byte signed integer)

Because the file header format is proprietary, the header has to date been only partially decoded. Nonetheless, the necessary information can be extracted to carry out the data conversion. This information reveals whether the data are in the MIZ-18 or MIZ-30 formats and the numbers of channels in the data file. Once these two pieces of information are determined, the conversion routine can retrieve and convert EC data files to a format suitable for any future analysis and evaluation. Figure 2.1 shows an intermediate display of the tools under conversion and segmentation functions that are activated from the main menu. After the conversion of raw data to a standard format, the code allows selection and possible modification of channel configuration information.

2.1.2 Automated Calibration and Display Algorithms

Calibration of raw EC data plays an important role in any data analysis procedure. Conventional phase angle calibration procedures for normalizing EC data are carried out manually and routinely involve visual alignment of the impedance-plane signal trajectory (i.e., lissajous plot) with respect to some reference indication. This implies that the extent of background fluctuations and signal-to-noise (S/N) ratio, as well as analyst judgment, could affect the calibration process and consequently lead to varying estimates of a desired parameter.

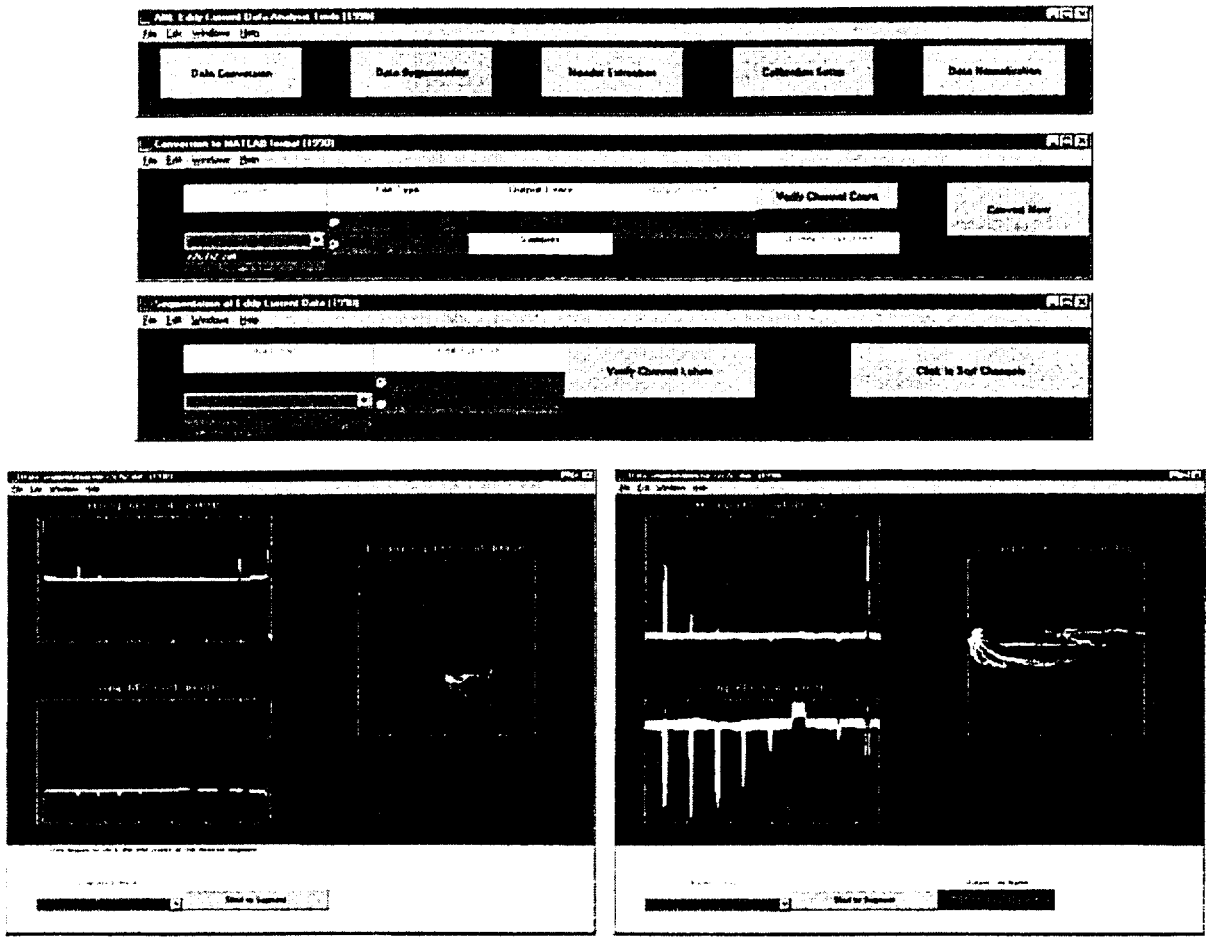

Fig. 2.1. MATLAB-based GUI tools have been implemented to allow direct conversion and segmentation of raw EC inspection results acquired with conventional commercial instruments for independent analysis.

Automatic calibration of multifrequency EC inspection results could provide more efficient data analysis and more important render consistent calibrations by reducing variability in analyst interpretation in the presence of noise (i.e., background fluctuations and artifacts). Algorithms for automatic calibration have been developed and incorporated into *ECTool* that display the acquired data in strip chart, lissajous, image, and isometric formats. Sample outputs of these programs are presented next.

Calibration of Bobbin and Rotating Coil Data. Signals from artifacts on a calibration standard tube are used to normalize the amplitude and phase of raw EC data. Amplitude scaling is performed with respect to peak signal voltage from a known indication on a calibration standard. Rotation of the phase angle at each frequency is calculated by using the lift-off signal and a second outer-diameter (OD) indication such as a simulated tube support plate (TSP) to determine the proper quadrants of the impedance-plane trajectory. When the lift-off signal cannot be detected reliably, incorporation of either a shallow inside-diameter (ID) indication or simulated lift-off artifact can improve the calibration results. Unlike conventional phase angle adjustments that are performed manually by visual alignment of the lissajous plot, the code uses a linear least-squares fit to multiple lift-off signals to estimate the phase angle. This

should improve the calibration accuracy, because the phase is typically not single-valued because it depends on such parameters as the condition of the tube inner-surface, sampling frequency, and probe alignment.

Figure 2.2a displays raw EC readings that were collected with the 2.92-mm (0.115-in.)-diameter unshielded primary pancake coil of a three-coil rotating probe on a groove standard. The code subsequently asks the user to interactively provide information on the approximate positions of a lift-off indication, a sound portion of the tube, and an amplitude scaling artifact; it calculates the phase angle rotation, null value, and scaling factors for uniform normalization of all of the data files that belong to the same calibration group. The calibrated RPC data are shown in Fig. 2.3a. Figure 2.3b shows typical output for a single channel when applied to bobbin coil readings on an ASME calibration standard. In this case, the differential signal amplitude was scaled with respect to the 20% OD flat-bottom holes (FBHs) to 4 V. All channels in the data set were calibrated in near-real-time. For more precise adjustment of bobbin phase angle, a thin layer of epoxy material was affixed on the inner surface of the calibration tube near one end to simulate the probe lift-off signal. The phase angle was then adjusted so the lift-off signal would be horizontal.

2.2 Visualization of RPC Data

A MATLAB program has been developed to display rotating probe c-scan data. It provides two views of the EC inspection results: two-dimensional (2-D) plan view (i.e., image format) and a four-dimensional (4-D) modified isometric view, which uses color mapping to display the additional relative phase information, unlike the conventional isometric plot, which provides only the amplitude information for a signal component. In its present form, it estimates the depth of a flaw by using an algorithm similar to that used in conventional analysis; however, instead of estimating depth at isolated points that are selected by the analyst, it does so over the whole region around the flaw and presents the results in terms of a color map. This approach improves the pattern recognition and makes it much easier to see the morphology of the cracking and seems to reduce the dependence on analyst judgment.

The program computes axial (in. or mm) and circumferential (in degrees) scaling of the data in accordance with a user-defined distance from two known markings on the tube. Helically scanned rotating probe data are automatically mapped to a rectangular grid by using the position information available from the trigger channel. In-phase and quadrature signal components at each frequency are subsequently processed and stored in a complex-number format for further manipulation. The 4–D modified isometric view has the advantage that it is relatively familiar to analysts accustomed to working with a conventional isometric plot, and simultaneously provides relative phase information for every point in the region that surrounds the flaw. For the image display, the depth of each indication is proportional to the intensity of each pixel. In the future, it is expected that the underlying algorithm could be improved by using techniques like multivariate regression analysis or neural-network analysis. Frequency and spatial-domain image enhancement and restoration algorithms are also being evaluated to improve plan view presentation of the results.

Figures 2.4a-c display typical outputs of the program. The data shown pertain to the 2.92-mm primary pancake coil of a three-coil RPC used to inspect 22.2-mm (0.875-in.)-diameter tubing. The image shown in Fig. 2.4b clearly displays the positions and shapes of all OD and ID

indications on the calibration standard tube. Figure 2.4(c), from top to bottom, displays the normalized data from the highest to the lowest available frequency. With the depth of penetration of eddy currents being proportional to the operating frequency, these image slices, in effect, represent radial cross sections of the tube. Screening of the c-scan inspection results in this manner would aid the determination of ID/OD aspects of an indication. Figure 2.5 is a c-scan image of another tube standard with axial and circumferential ID and OD electro-discharge-machined (EDM) notches. Once again, the shape and orientation of each indication closely matches the corresponding artifact on the tube. Finally, Figs. 2.6 and 2.7 show a series of image displays for circumferential and axial indications from representative laboratory-grown specimens from the ANL tube bundle mock-up. Despite the fact that all indications were in the roll transition region of the tube, in all cases, the shape and extent of indications are clearly resolvable.

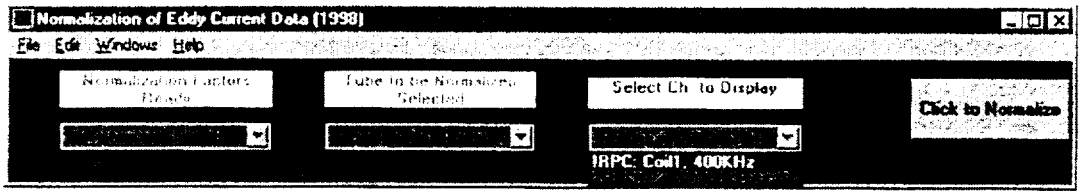

(a)

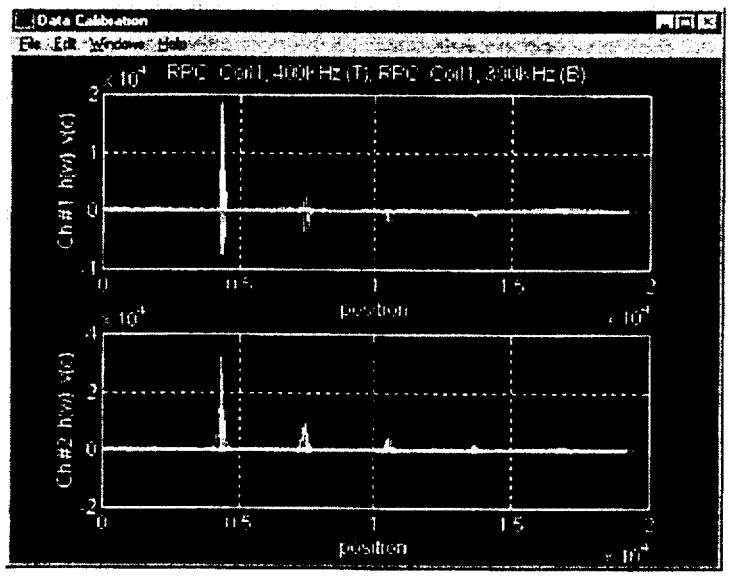

(b)

Fig. 2.2. Typical display of (a) data calibration GUI tool and (b) strip chart display of raw EC inspection results by data calibration function of ECTool. Measurements were made on groove standard with 2.92-mm (0.115-in.)-diameter primary pancake coil of a three-coil rotating probe.

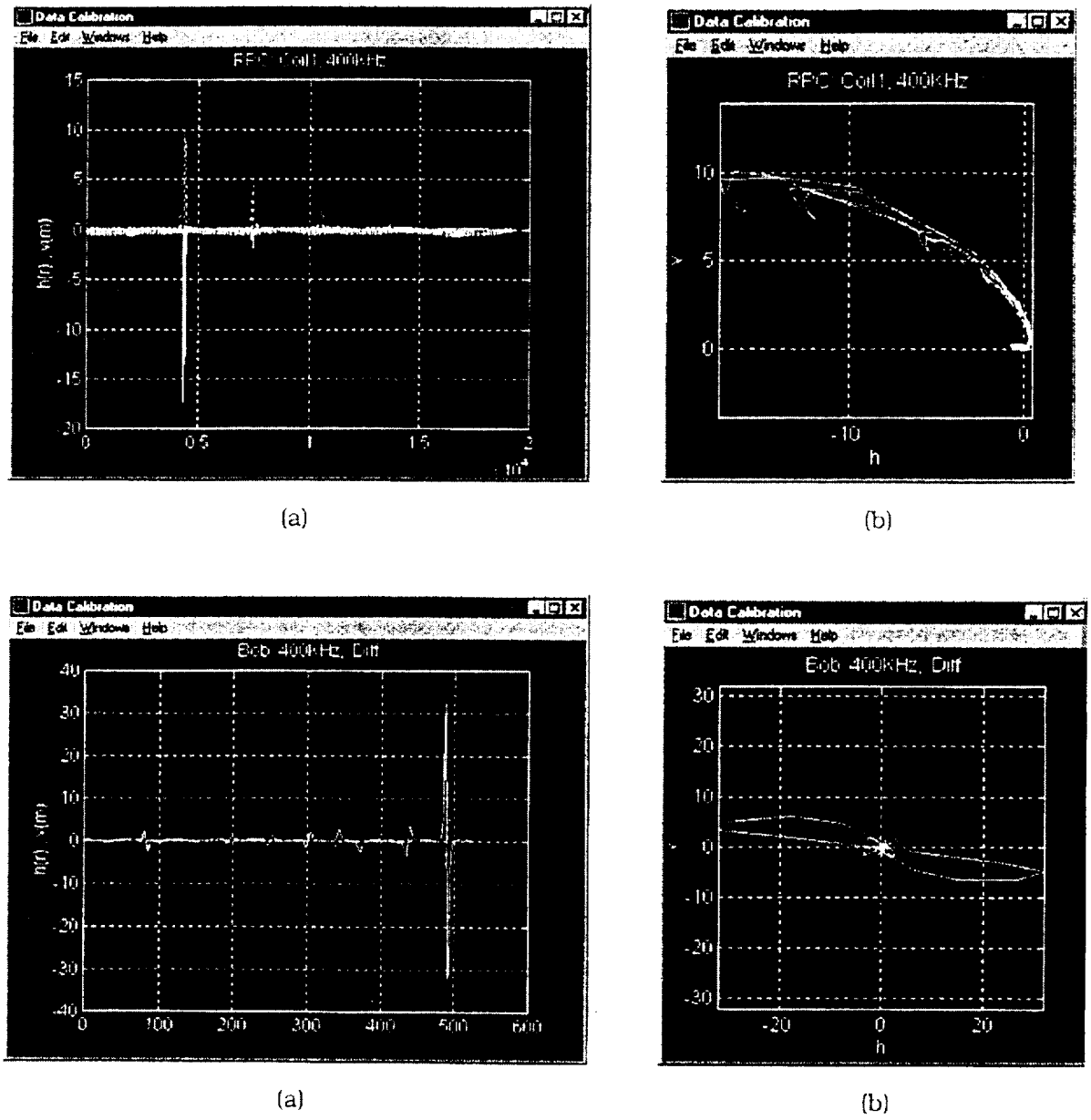

(a) (b)

(a) (b)

Fig. 2.3. Typical (a) strip chart and (b) lissajous pattern display of calibrated EC inspection results by data calibration function of ECTool GUI. Measurements were made on (top) groove standard with 2.92-mm (0.115-in.)-diameter primary pancake coil of a three-coil rotating probe and (bottom) ASME standard with 18.4-mm (0.725-in.) -diameter bobbin probe.

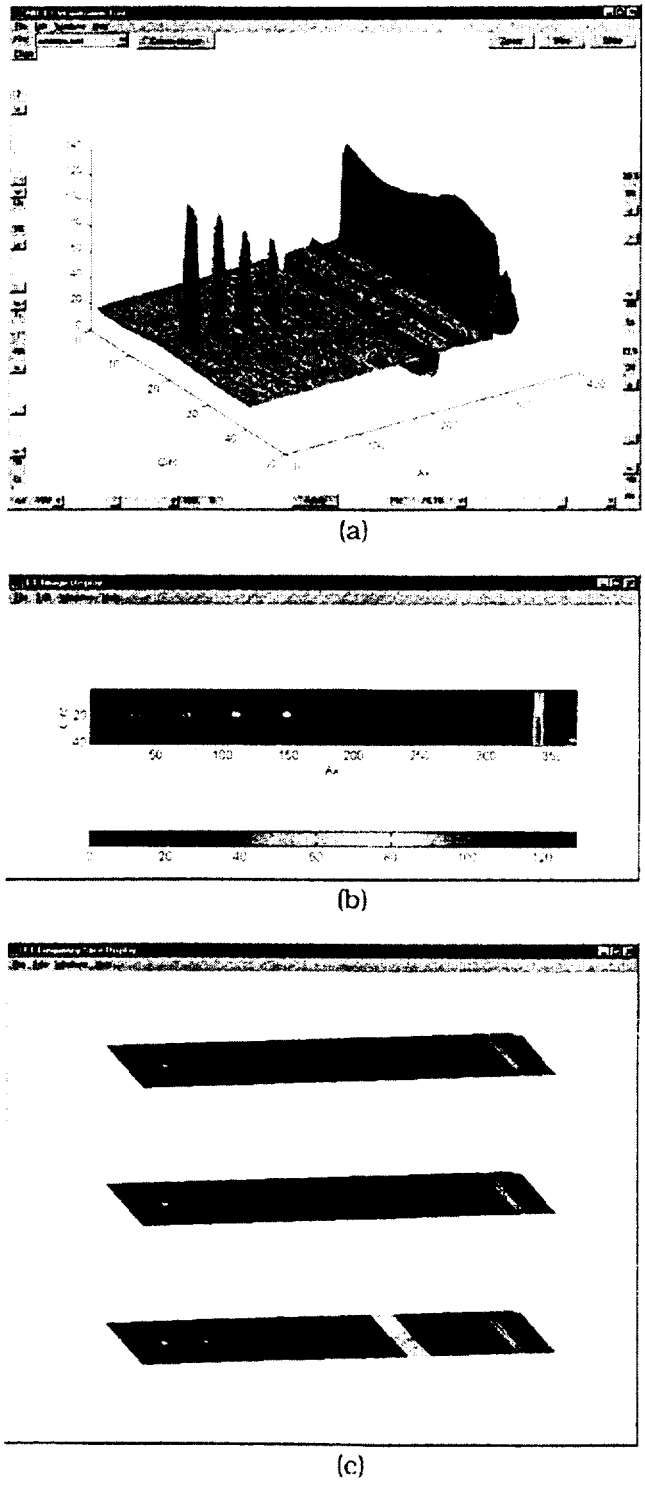

Fig. 2.4. Outputs of data visualization tool showing (a) mesh plot, (b) image display, (c) frequency slice display of ASME standard tube. Indications from left to right consist of 100%, 80%, 60%, 40%, four 20% OD FBHs, simulated TSP, 10% OD and 20% ID circumferential notches.

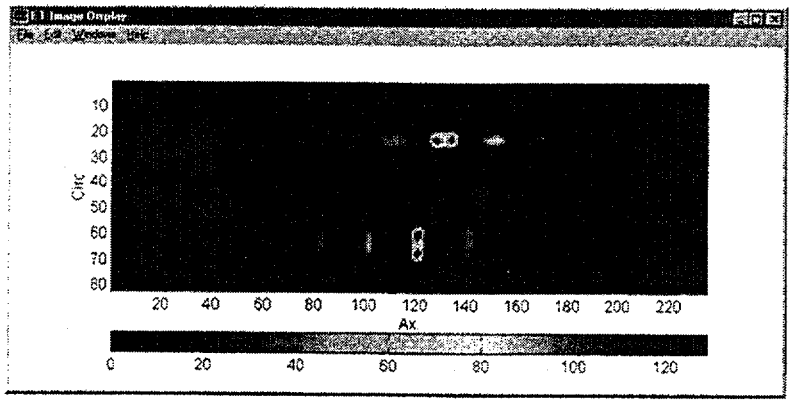

Fig. 2.5. Output of data visualization tool showing image of tube standard with 6.35-mm (0.25-in.)-long axial and circumferential ID and OD notches.

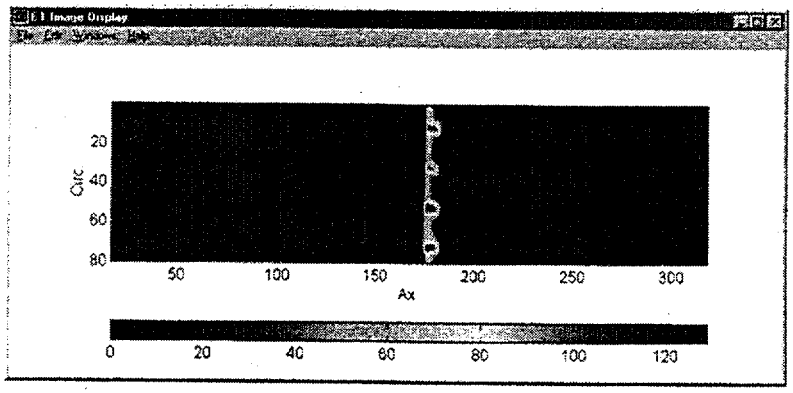

(a)

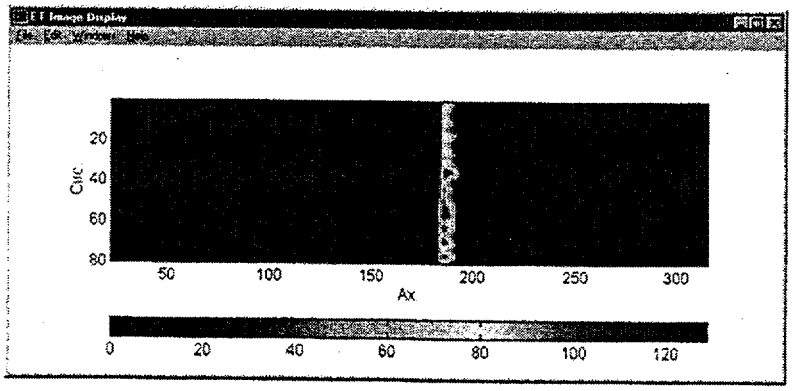

(b)

Fig. 2.6. Output of data visualization tool showing image of mock-up tube specimens with longitudinal IDSCC indications at roll transition region. Indications consist of (a) four through-wall cracking regions and (b) multiple axial cracks with ≈80% maximum depth.

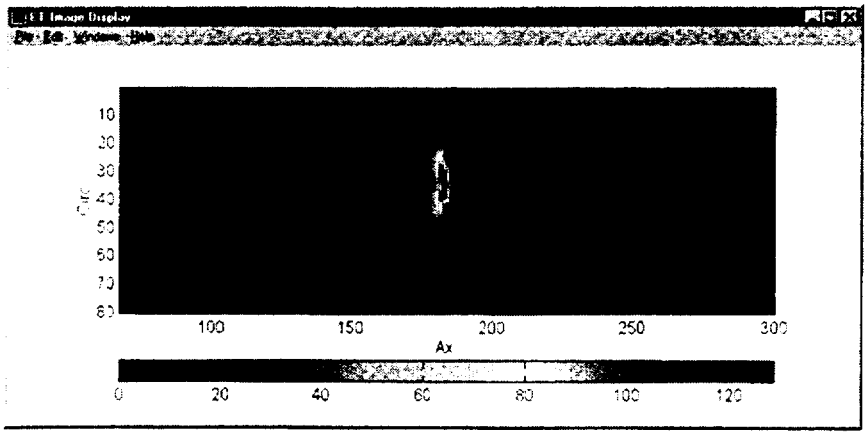

(a)

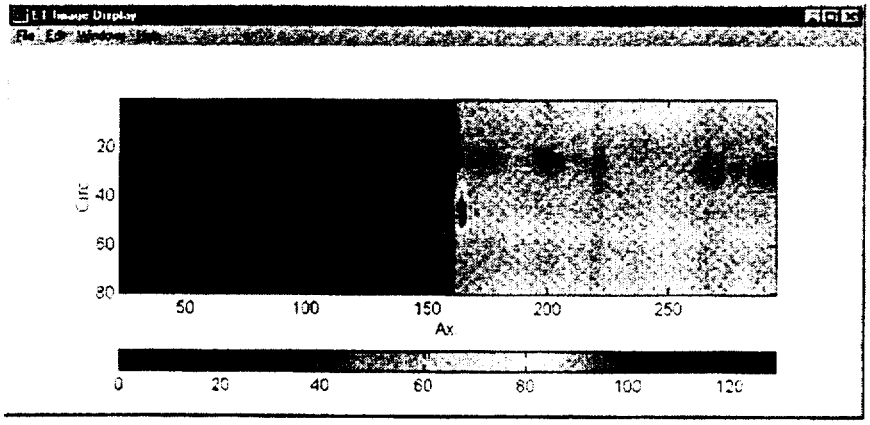

(b)

Fig. 2.7. Output of data visualization tool showing image of mock-up tube specimens with circumferential ODSCC indications at roll transition region. Indications consist of (a) two adjacent parallel cracks with maximum depth of ≈90% OD, and (b) a single crack of ≈60% OD.

2.3 Application of Digital Filters

Analog and digital filters are often integral parts of any electronic measurement device. They can be implemented either in the hardware or software and help discriminate between real signals and noise. Frequency domain bandpass finite-impulse response (FIR) digital filters are nonrecursive filters that offer certain advantages and limitations over recursive infinite-duration impulse response (IIR) filters. The primary advantages are their linear phase, stability, finite-duration transients, and efficiency of implementation. FIR filters are always stable, but require longer sequences to meet the same requirements as their IIR counterparts. This latter property, a direct consequence of their simpler transfer function, often translates into more computation time for nonrecursive filters. As with all frequency-domain filters, when conditions are not ideal, the increase in S/N ratio gained by the filtering process is always accompanied by various degrees of perturbation of amplitude and phase of the original signal.

The time-domain difference equation for a linear filter with input sequence *x(k)* and output sequence *y(n)* could be written in a general form as

$$y(n) = \sum_{k=0}^{M} b(k)\,x(n-k) + \sum_{k=1}^{N} a(k)\,y(n-k), \tag{2.1}$$

in which the coefficients a and b define the filter response. The transfer function of the IIR filter in z domain, which is the z-transform of the time-domain difference Eq. 2.1, can be described by the following equation

$$H(z) = \frac{Y(z)}{X(z)} = \frac{\sum_{k=0}^{M} b(k)z^{-k}}{a_0 + \sum_{k=1}^{N} a(k)z^{-k}}, \tag{2.2}$$

where $a_0 = 1$ for the case of a FIR filter, and the summation in the denominator of Eq. 2.2 vanishes. The difference between the two types of filters can be seen by examining the filter frequency response, which is a rational function in z^{-1} for an IIR filter and represents a discrete Fourier transform for a FIR filter. Regardless of filter type, unless the data sequence in the Fourier domain is composed of sinusoidal components of the desired signal and noise that are well separated, the amplitude and phase of the filtered signal will always experience perturbation with respect to those of the original signal. This is of particular concern in the case of EC signals in which the frequency content of the entire data sequence is often closely spaced and thus requires very sharp (high-order) filters to separate real signals from background variations.

The use of FIR filters to improve the S/N ratio of bobbin probe data was examined. Figure 2.8 shows a typical transfer function for the FIR filters of interest. The sampling frequency for the raw EC data was taken to be 400 Hz (twice the Nyquist frequency). The transfer function was constructed by using 50th-order lowpass and 100th-order highpass filters that are subsequently applied to the signal. Although a single bandpass filter could be implemented to meet similar cut-off requirements, such a filter would be less efficient because of its symmetric transfer function. High-pass filters for EC signal conditioning often require a sharper rising edge and consequently a larger number of coefficients, because much of the useful information content of the Fourier domain spectrum is at the low-frequency end.

Figures 2.9a and b show the power spectral densities that were used to determine the filter pass band for the differential and absolute bobbin coil signals for a TSP indication. Figures 2.10 and 2.11 show a set of original and filtered data segments at f = 400 kHz. In both cases, the original differential and absolute signals contain large background fluctuations. The S/N ratio of the filtered data segment in all cases has improved substantially when compared with the original data. On the other hand, the filtered horizontal and vertical components do not exhibit the identical phase relationship of the original data. Preliminary assessment of the results suggests that frequency domain filters are generally more suitable for improving detection probability. Phase angle perturbations that are a result of filter application can often lead to more complex impedance-plane trajectories, which could complicate conventional data analysis procedures that rely on phase angle information.

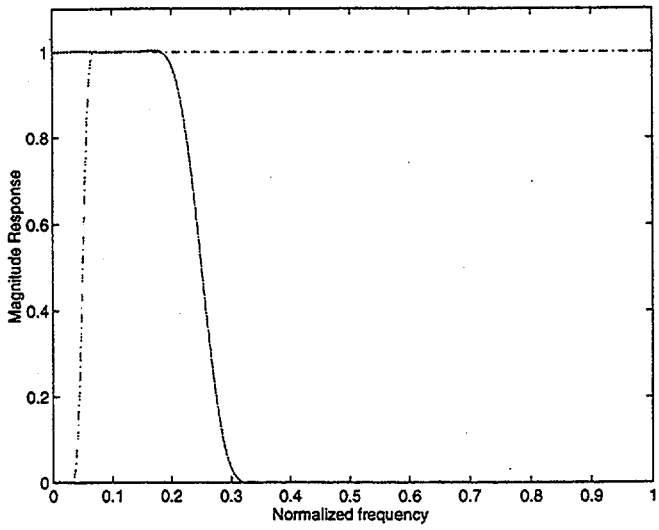

Fig. 2.8. Transfer function of bandpass FIR filter composed of 50th-order low-pass (solid line) and 100th-order high-pass (dashed line) filters (Nyquist frequency = 1).

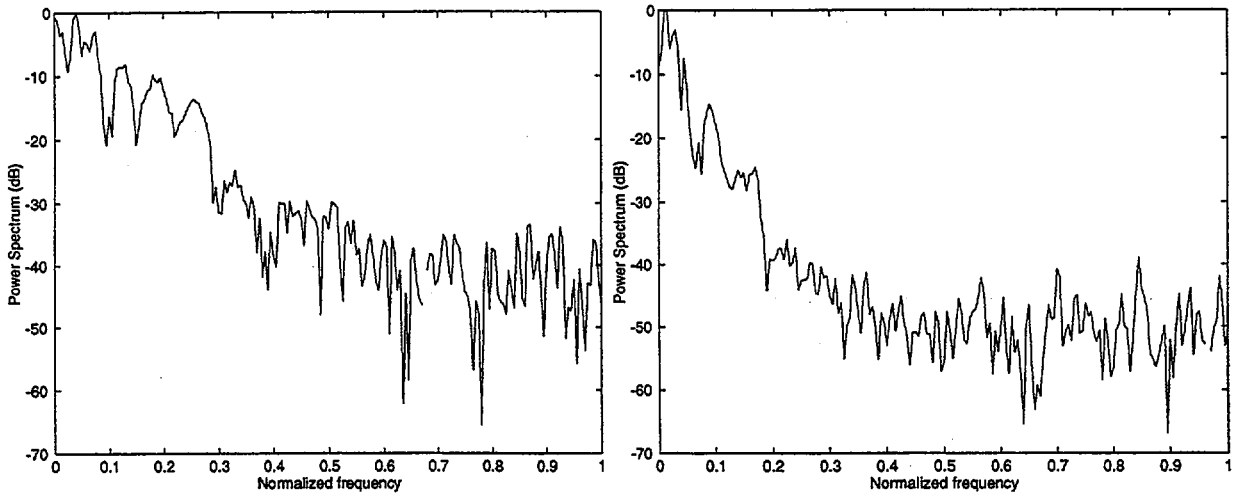

Fig. 2.9. Power spectral density (Nyquist frequency = 1) of 400 kHz (a) differential and (b) absolute bobbin coil signal for TSP indication.

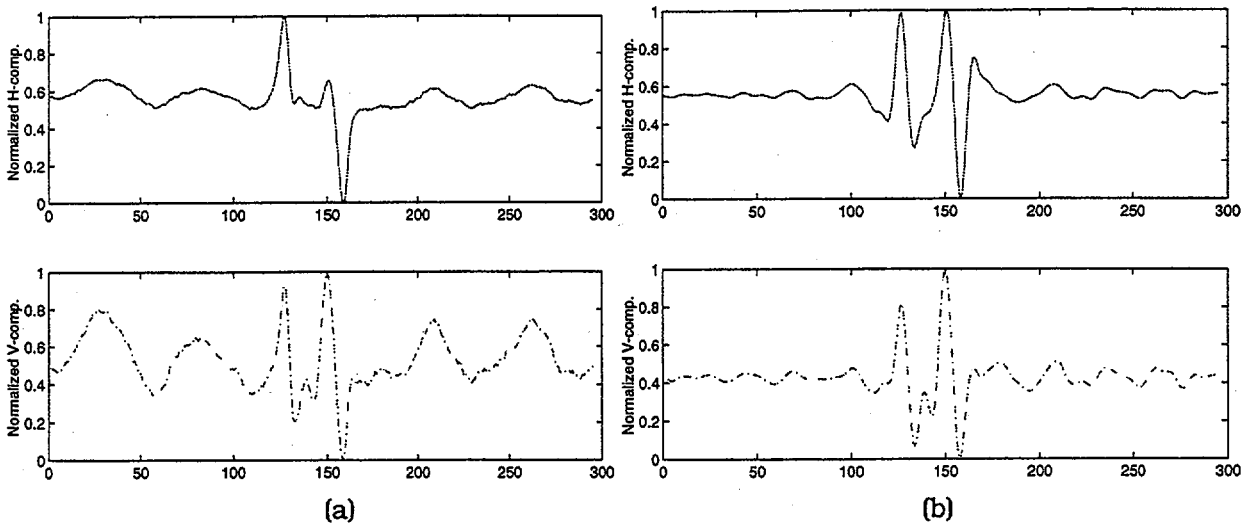

Fig. 2.10. Normalized horizontal and vertical components of (a) original and (b) filtered differential bobbin coil signal for TSP indication at 400 kHz. Horizontal axis shows data points along the tube axis.

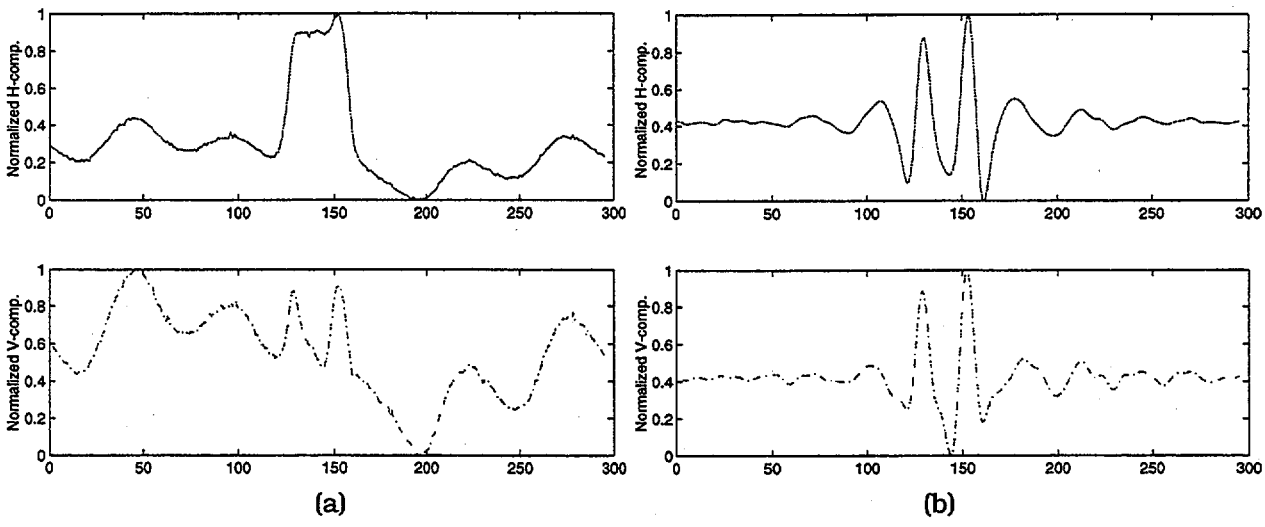

Fig. 2.11. Normalized horizontal and vertical components of (a) original and (b) filtered absolute bobbin coil signal for TSP indication at 400 kHz. Horizontal axis shows data points along the tube axis.

3 Data Analysis

Linear and nonlinear multivariate analysis techniques have been used to develop models that correlate EC NDE results with flaw size and tube failure pressure. The robustness and range of applicability of such correlation models is limited by the range of degradation morphologies and inspection artifacts in the corresponding data base. It is expected that these correlations will be revised and updated as additional data are developed in the course of the program or become available from other sources.

3.1 Depth Sizing

Multivariate models for analysis of RPC data to estimate flaw depth have been developed. Both neural-network and multiparameter linear regression models have been considered.

3.1.1 Improvement of Back-Propagation Algorithm for Flaw Sizing

The use of a standard back-propagation neural-network structure with momentum to train a feed-forward network to predict flaw depth has been studied. This work is an extension of work reported in Ref. 1. The data base used to train the network contained two EDM standards and 19 tubes with laboratory–grown defects. These tubes, fabricated from Alloy 600, with tube OD of 22.2 mm (0.875 in.) and a wall thickness of 1.27 mm (0.05 in.), all containing outer surface defects, were obtained from the Pacific Northwest National Laboratory (PNNL). Thirteen of the tubes contained axial ODSCC, four tubes contained circumferential ODSCC, and two tubes exhibited IGA degradation. The EDM notch standards contained both circumferential grooves and axial notches. Nominal notch depths were 20, 40, 60, 80, and 100% throughwall (TW) for both standards. The specimens with cracks have been examined by metallography to determine the "true" crack depth.[2] Table 3.1 lists the specimens in the data set. The data were recorded at 65, 130, 260, and 520 kHz, every 0.75mm (≈0.03 in.) along the tube axis by using a rotating probe with a P90 pancake coil. Readings were made every 22.5° around the circumference, simulating a 16-coil array configuration.

Because the optimization function for neural networks is often highly nonlinear, training can converge to a local rather than the desired global minimum. To overcome this obstacle, momentum was introduced to allow the network to escape shallow minima. This procedure often does not provide the most efficient computation time, although shorter training times are always desirable. One way to achieve shorter training time, keeping the convergence criteria intact (tolerance on the solution accuracy), is to use a variable learning rate that attempts to keep the learning step size as large as possible while keeping learning stable. However, effective control of the size of the learning step can be difficult. One promising alternative is the Levenberg-Marquardt optimization method. This algorithm is more sophisticated than the simple gradient descent used in backpropagation. Data analyses were performed on a test set that was described in an earlier report.[1] Depth prediction results suggest that the performance of the neural-network that was trained according to the Levenberg-Marquardt method is comparable to the performance of one trained with the backpropagation method. However, when compared with backpropagation, only a fraction of the training time is required to satisfy similar convergence criteria.

Table 3.1 Summary of tube samples used for neural-network studies.

Tube Name	Defect Type[a]	Usable Points[b]
vbs003d.dat	Standard	625
vbm001.dat	Standard	575
vbm002.dat	Standard	575
vbm003.dat	Standard	575
vbm004.dat	Standard	575
vbm005.dat	Standard	575
vbm006.dat	Standard	575
vbm007.dat	Standard	575
vbm008.dat	Standard	575
vbm009.dat	Standard	575
vbm010.dat	Standard	575
vbm011.dat	Standard	575
vbm012.dat	Standard	575
5-01	IGA	2573
5-14	IGA	2130
4-11	CODSCC	685
w-23-03	CODSCC	2875
w-23-09	CODSCC	1215
w-40-07	CODSCC	2796
2-05	LODSCC	302
b-10-02	LODSCC	2045
b-10-10	LODSCC	1433
b-30-02	LODSCC	990
b-45-06	LODSCC	875
b-49-05	LODSCC	798
b-49-09	LODSCC	102
b-55-08	LODSCC	3057
b-59-10	LODSCC	2557
b-62-09	LODSCC	1380
b-63-07	LODSCC	83
e-13-06	LODSCC	2646
1-14-06	LODSCC	3257
TOTAL		39,290

[a] CODSCC: circumferential ODSCC; LODSCC: longitudinal ODSCC

[b] "Usable Points" indicates that a corresponding metallographic depth was available for the EC measurement.

Selection of Training Sample. Because it is important to estimate larger defect depths with better accuracy, the criterion for selecting training data was weighted to ensure that the training population emphasized the nonlinear mapping between EC measurement and defect depth. The weighting method can be described as follows: Let D be the defect depth (normalized by the tube wall thickness) of a training sample candidate, and let θ be a threshold value in the range [0, 1] and U a random variable with uniform distribution in the range [0, 1]. Then the training sample will be included in the training population (i.e., higher weight for greater defect depth) if $D \geq \theta \times U$. For example, selecting θ = 0.6 allows all available samples with a defect depth of 60% or greater to be selected, while a sample with defect depth of 20% will have a 33% chance of being selected as a member of the training population.

Table 3.2 summarizes the performance of the neural-network that was based on training populations with various threshold values. The candidate training sample set comprised all of the EC measurement and defect depth pairs in the test set except the five indications that were to be predicted. A threshold value of 0.0 is equivalent to using the entire training sample set for training. The sizing accuracy of the predicted tubes fluctuates with the threshold value (i.e., composition of the training population). The results in Table 3.2 suggest that prediction accuracy is optimized when the threshold value is ≈0.5. The accuracy obtained with a threshold value of 0.5 is comparable to that obtained with a value of 0.0, and the training can be accomplished in a much shorter time because fewer indications are actually used for training. Another potential advantage of using a threshold value > 0.0 is that undesired variations in EC measurements caused by artifacts, such as TSP, may be reduced because only a portion of the defect-free data will be included. The results in Table 3.2 were obtained with 12 hidden-layer nodes. Table 3.3 shows results that were obtained when the network contained 10 hidden-layer nodes and all other conditions were the same as those in Table 3.2. In this case again a threshold value of ≈0.5 seems to give the best results.

Effects of Nonlinear Transfer Function. The structure of a neural-network can significantly influence its performance. In this study, the effect of the type of neuron transfer function on the performance of neural-network algorithm discussed earlier was evaluated. Specifically, two most commonly used transfer functions for mapping neuron input to its output were examined. These transfer functions can be expressed as

$$\tan sig(x) = \frac{\left(1 - e^{-x}\right)}{\left(1 + e^{-x}\right)} \tag{3.1}$$

and

$$\log sig(x) = \frac{1}{\left(1 + e^{-x}\right)}. \tag{3.2}$$

The function *tansig* maps the input range (-∞,∞) to output range (-1,1), whereas *logsig* maps the same input range to (0,1). Because the desired output in this study is the degradation depth in percentage of the tube wall thickness, Eq. 3.2 seems more suitable for the output layer neurons. The effect of using either Eqs. 3.1 or 3.2 at the first layer was examined by comparing the accuracy of the defect depth prediction. Table 3.4 summarizes the results of this analysis

for a network with 12 hidden nodes. The parameter θ again controls the selection of the training data.

Table 3.2 Depths[a] predicted by trained neural-network with training samples of various threshold values. The network contains 12 hidden layer nodes; the training set contained 17 specimens.

Tube Name	Defect Type[b]	Predicted depth with θ = 0.0	0.3	0.5	0.8	1.0	Actual Depth[c]
4-11	CODSCC	100	31	99	60	61	100
B-10-10	LODSCC	46	51	41	43	43	43
B-63-07	LODSCC	70	59	65	57	62	69
E-13-06	LODSCC	15	26	21	23	17	0
vbm005	standard	75	73	73	76	73	75

[a] Values shown are maximum depths as percentage of tube wall thickness.
[b] CODSCC: circumferential ODSCC; LODSCC: longitudinal ODSCC.
[c] Obtained by metallography.

Table 3.3 Depths[a] predicted by trained neural-network with training samples of various threshold values. The network contains 10 hidden layer nodes.

Tube Name	Defect Type[b]	Predicted depth with θ = 0.0	0.3	0.5	0.8	1.0	Actual Depth[c]
4-11	CODSCC	31	56	93	46	52	100
B-10-10	LODSCC	45	48	46	48	42	43
B-63-07	LODSCC	54	67	63	66	69	69
E-13-06	LODSCC	18	32	27	26	30	0
vbm005	standard	73	91	74	73	74	75

[a] Values shown are maximum depths as percentage of tube wall thickness.
[b] CODSCC: circumferential ODSCC; LODSCC: longitudinal ODSCC.
[c] Obtained by metallography.

The results suggest that both forms of the neuron transfer function yield comparable defect depth predictions. However, when the *logsig* transfer function is used, a network with randomly initialized weights sometimes cannot be trained successfully, i.e., the initial weight vector cannot be updated to escape a local minimum of the optimization criterion. This phenomenon was never observed when the *tansig* transfer function was used at the first layer. Table 3.5 summarizes the frequencies at which the network fails to be trained properly with these two transfer functions at the first layer. A failed network is expected to produce a zero depth estimate for all indications.

Number of Hidden-Layer Neurons. The optimal number of hidden-layer neurons depends on the complexity of the relationships between input-output pairs presented to the neural-

network. A neural-network with a smaller number of hidden-layer nodes may not exhibit sufficient input-output complexity to deduce a useful relationship between measured NDE parameters and defect depth. On the other hand, an arbitrarily chosen large number of hidden-layer neurons could introduce additional nonlinearity to the structure. Such additional nonlinearity makes the optimization function of the network more complex and thus increases the probability for the training process to be trapped in local minima.

Tables 3.2 and 3.3 and Tables 3.4 and 3.6 can be used to compare predictions for networks with 12 hidden-layer neurons with predictions from networks with 10 hidden-layer neurons. Reducing the number of hidden-layer neurons from 12 to 10 does not seem to affect the performance of the trained network. For similar convergence criteria, because the network with a smaller number of hidden-layer neurons could be trained more efficiently, these results suggest that 10 hidden-layer neurons are preferred over 12. It should be noted, however, that the optimal size of hidden-layer neurons could also depend on the measurement technique and probe characteristics.

Table 3.4. Depths[a] predicted by trained neural-network with two types of nonlinear transfer functions for first layer and two threshold values of θ for selecting each training specimen. Network contains 12 hidden-layer nodes.

Tube Name	Predicted Depth θ = 0.0 *logsig*	θ = 0.0 *tansig*	θ = 0.5 *logsig*	θ = 0.5 *tansig*	Actual Depth[b]
4-11	93	75	99	100	100
B-10-10	52	39	49	60	46
B-63-07	58	71	62	67	69
E-13-06	22	27	30	44	0
vbm005	97	73	87	77	75

[a] Values shown are maximum depths as percentage of tube wall thickness.
[b] Obtained by metallography.

Table 3.5. Frequency of unsuccessful training of neural-network with random initialization of weight vectors and two types of first-layer neuron transfer functions. Total training conducted for each hidden node condition is 50.

Hidden nodes	4	6	8	10	12
logsig(.)	0.08	0.04	0.04	0.08	0.08
tansig(.)	0.0	0.0	0.0	0.0	0.0

Table 3.6. Depths[a] predicted by trained neural-network with two types of nonlinear transfer functions for first layer and two threshold values of θ for selection of training samples. Network contained 10 hidden-layer nodes.

Tube Name	Predicted Depth θ = 0.0 *logsig*	θ = 0.0 *tansig*	θ = 0.5 *logsig*	θ = 0.5 *tansig*	Actual Depth[b]
4-11	97	94	64	97	100
B-10-10	45	52	43	97	46
B-63-07	64	60	65	70	69
E-13-06	24	32	33	55	0
vbm005	90	73	74	84	75

[a] Values shown are maximum depths as percentage of tube wall thickness.
[b] Obtained by metallography.

3.1.2 Multivariate Regression Analysis

Three distinct multivariate regression algorithms have been evaluated as alternatives to neural-network structures for the development of correlations between EC data and flaw size and tube failure pressure. The three approaches consisted of multiple linear regression (MLR), principal component regression (PCR), and partial least squares (PLS) techniques. To date, PLS has been shown to be the most versatile of the three techniques for EC data analysis.

Regression Algorithms. Multivariate analysis techniques are often utilized to explore unknown trends in large quantities of data. The two basic stages in such analyses are generally referred to as calibration and prediction. In calibration stage, a data matrix is constructed from the probe response at various time or frequency slots for a given set of calibration samples. The calibration phase produces a model that relates the probe response to known values of the parameters to be estimated. In the prediction stage, the matrix of coefficients and weights that describes the system response (input-output relationships) is used to estimate the parameters of interest in new measurement test sets. Of the three multivariate techniques, MLR, an extension of the ordinary least squares algorithm, is used most frequently. Having the response matrix [X] and the parameter matrix [Y], MLR develops a linear combination of variables in [X] that minimizes the errors in reproducing [Y]. This is accomplished by constructing a relationship between [X] and [Y] such that

$$[Y] = [X][\beta] + [E], \tag{3.3}$$

where $[\beta]$ is the matrix of regression coefficients and [E] is the matrix of errors associated with the MLR model. The matrix $[\beta]$ is found by linear regression to minimize the difference between the true and estimated elements of the parameter matrix in a least squares sense as

$$[E] = \sum_{n=1}^{N} \sum_{m=1}^{M} (y_{mn} - \hat{y}_{mn})^2 = \sum_{n=1}^{N} \sum_{m=1}^{M} \varepsilon_{mn}^2 . \tag{3.4}$$

The MLR approach is often a good choice when dealing with linear systems that are described as exhibiting linear response, low noise, no interference, and no colinearities. However, when the EC inspection data discussed in Sec. 3.1.1 were analyzed by MLR, the correlations that were developed initially were not always satisfactory because of external artifacts, background fluctuations, and colinearities in instrument response at various frequencies. MLR attempts to use all of the available information in the independent variable matrix for model construction. Both relevant (signal) and irrelevant (noise) information will be weighted equally by this method when input-output relations are constructed. To overcome this limitation, the two factor-based techniques (PCR and PLS) were subsequently examined. The factors are linear combinations of the original variables. Factor-based models attempt to use a minimal set of factors that best describe the true relationship between the independent and dependent variable matrix. Because factor-based models do not attempt to directly invert the covariance matrix, potential colinearities in data could be accommodated without causing singularities.

PLS was chosen to construct a multivariate regression model for the EC data. For the PLS algorithm, a general model would consist of a regression between the scores of the relationships for the dependent variable [Y] and independent variable [X]. The outer relationships can be written in matrix form as

$$[X] = [T][P] + [E] = \sum_{n=1}^{N} t_n p_n + [E] \tag{3.5}$$

$$[Y] = [U][Q] + [F] = \sum_{n=1}^{N} u_n q_n + [F], \tag{3.6}$$

with the inner relation defined by

$$\hat{u} = b_n t_n, \tag{3.7}$$

where [T], [U], [P], and [Q] are the eigenvectors and eigenvalue matrices and [B] is the vector that contains the inner relationships. The principal components are simultaneously calculated for both blocks. The intention is to minimize $\|F\|$ (i.e., $Norm\{[F]\}$), and hence to construct a useful relationship between [X] and [Y].

Preliminary results are shown next for implementation of a PLS algorithm to estimate degradation depth for the tube data set described in Sec. 3.1.1. Once again, the NDE parameters consisted of horizontal and vertical components of the measured signal at four frequencies. A MATLAB program was written to carry out the multivariate analysis. Unlike the nonlinear analyses described in earlier sections, calibration and prediction with this approach can be carried out in real time. In the initial calibration stage, the code calculates the weight and coefficient matrices from a user-defined set of normalized data files. Estimated depths are then sequentially calculated for each test specimen and profiles are displayed as a function of position along the tube. Because the available data set analyzed in this study contains only OD indications, a single-output depth profile was estimated for each tube specimen. Estimated depth profiles can be displayed simultaneously by the code for both OD and ID indications.

Figures 3.1-3.5 display representative EC traces of the available standard and defect-containing tube specimens. Figures 3.1 and 3.2 show the normalized horizontal and vertical components of data for the standard tubes with axial and circumferential defects, respectively. Several measurements of the standard with circumferential grooves were available in which a simulated OD ferrite support ring was placed at various locations on the tube. Figures 3.3-3.5 show signal components at the highest frequency for representative tubes that contained longitudinal ODSCC, circumferential ODSCC, and IGA degradations, respectively. The inspection data from all of the specimens in this set showed a variable but generally high level of noise. The noise level is somewhat atypical; its source is not known, but could be either the manufacturing process or the treatment of the tubes when defects were created.

Various calibration and prediction scenarios were examined. Results are presented here for the case in which the calibration/training is based primarily on the tube standards. For the first test case, all of the data on the two calibration standard tubes with axial and circumferential defects were used in the training stage. For the second test case, two specimens with shallow OD indications were added to the training data set to improve noise suppression.

Figure 3.6 shows the plot of maximum measured vs. estimated depth when the training set consisted of all the available tube standard data files. Figure 3.7 shows the results when two specimens with shallow OD indications were added to the training set to help suppress the excessive noise in these tubes. Comparison of Figs. 3.6 and 3.7 indicates that the addition of the OD indications helped eliminate artifacts and improved the overall estimation of the depths for the entire range of available degradation morphologies. Results of the second test also indicate less scattering of estimated maximum depths and better correlation of measured and predicted depths. Training exclusively on circumferential and axial notches appears to lead to underestimation of shallower OD indications. In both cases, the multivariate model was able to effectively suppress background variations and indications from simulated tube support and ferrite rings.

The choice of the EC probe configuration strongly affects the results of the analysis. As stated earlier, the P90 coil that was utilized to inspect tube specimens was selected to try to provide an optimal trade-off between circumferential coverage (when used in 16-coil array configuration) and sensitivity. Examination of all signal traces in the data set generally indicates a lack of probe resolution and insensitivity (i.e., low S/N ratio) to shallow OD degradations (e.g., Figs. 3.3 and 3.5). Inasmuch as EC indications are proportional to the degree that the paths of induced currents are perturbed by the defect, small isolated indications, which seem to be characteristic of at least some of the specimens, would be expected to produce low S/N ratios which, in turn, could lead to underestimation of degradation depth. Sensitivity and resolution could be improved by using smaller coils. The penalty for the higher resolution achieved with the smaller rotating probes is reduced inspection speed and additional inspection data. Multivariate analysis for sizing with smaller rotating probes is currently under study.

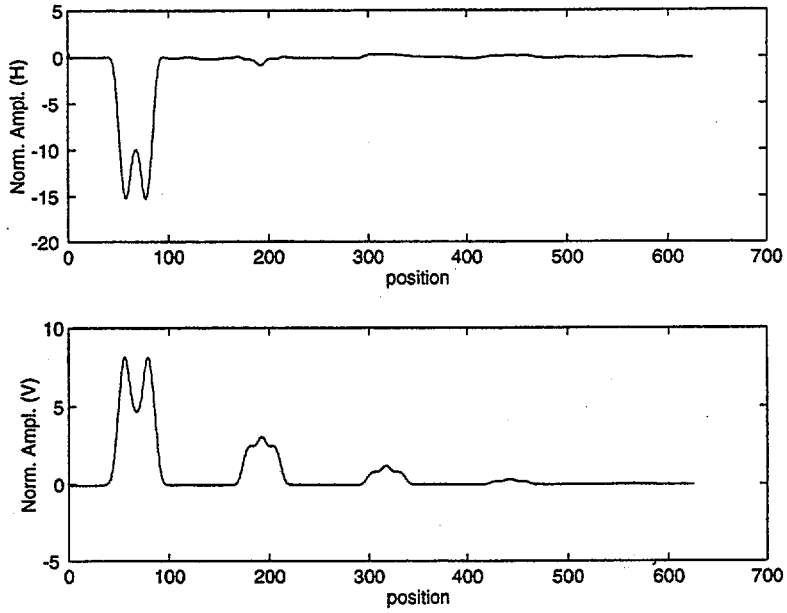

Fig. 3.1. Normalized horizontal and vertical components of EC inspection data for tube standard that contained axial notches.

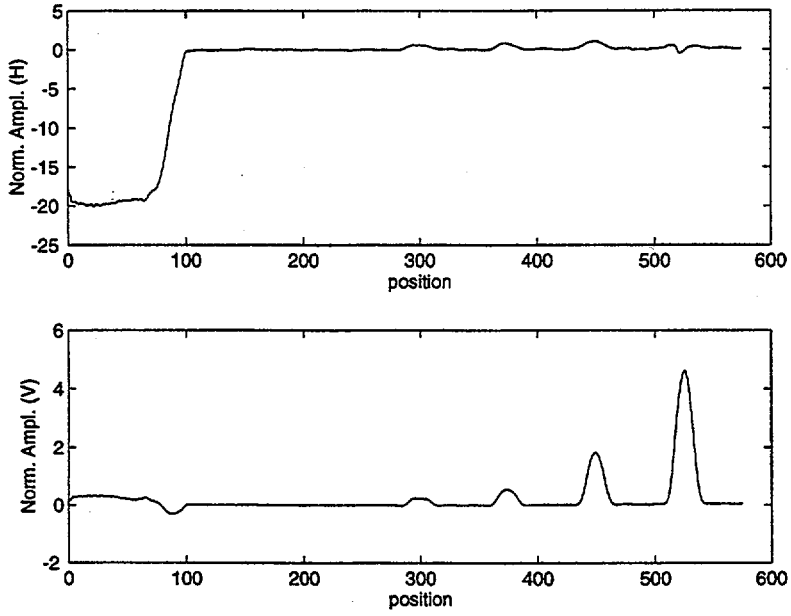

Fig. 3.2. Normalized horizontal and vertical components of EC inspection data for the tube standard that contained circumferential grooves.

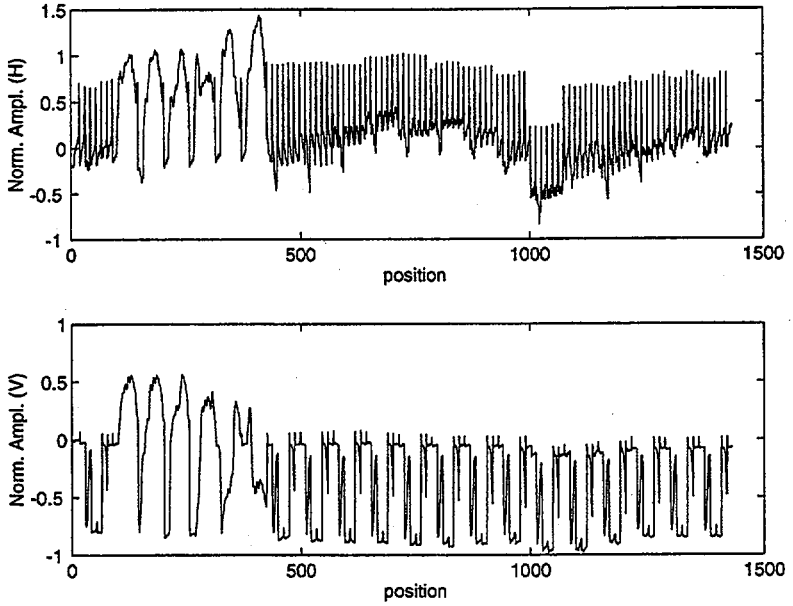

Fig. 3.3. Normalized traces of horizontal and vertical components of EC inspection data for representative specimen with longitudinal ODSCC degradation.

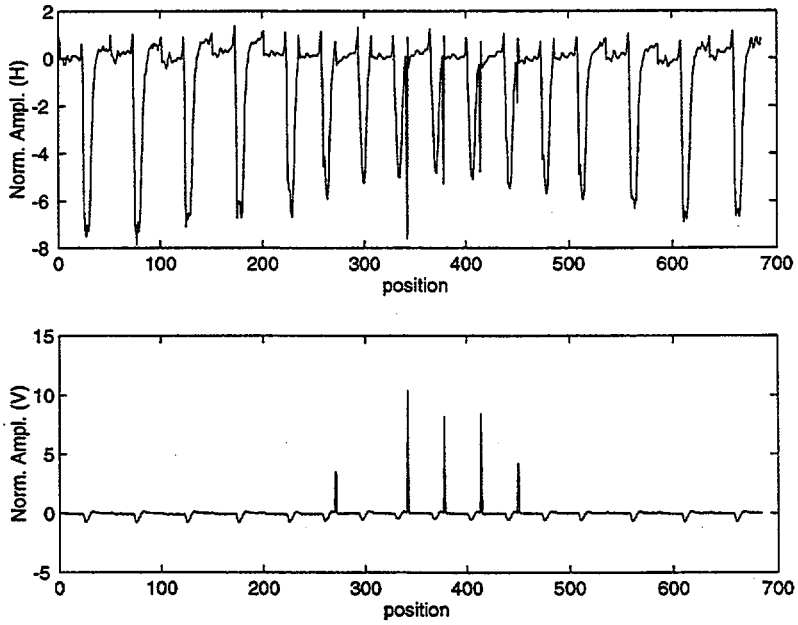

Fig. 3.4. Normalized traces of horizontal and vertical components of EC inspection data for representative specimen with circumferential ODSCC degradation.

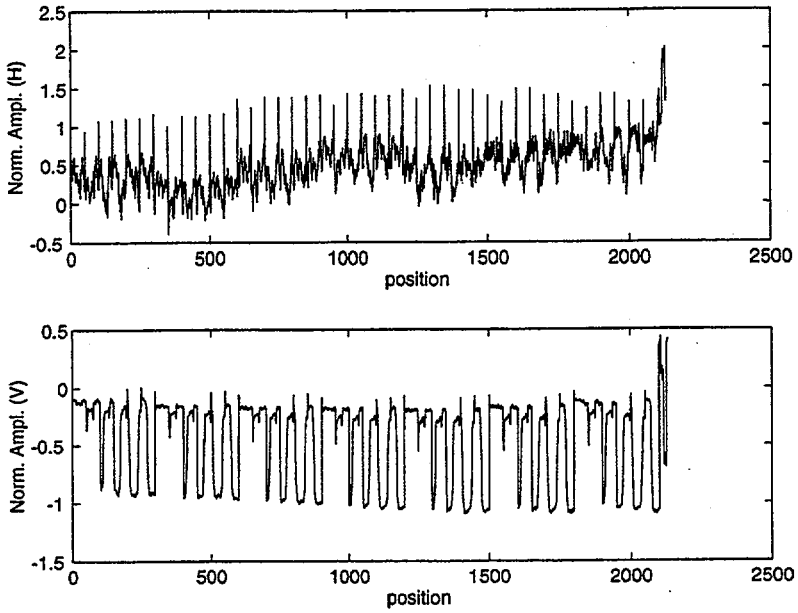

Fig. 3.5. Normalized traces of horizontal and vertical components of EC inspection data for representative specimen with IGA degradation.

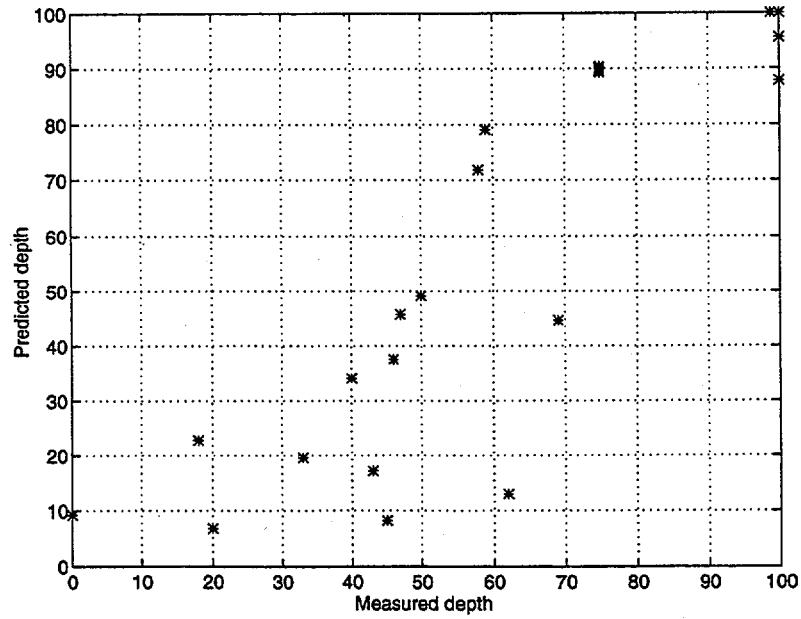

Fig. 3.6. Maximum measured vs. predicted depth in percent of wall thickness for all available specimens when training set consisted of all calibration standard tubes with simulated axial and circumferential notches.

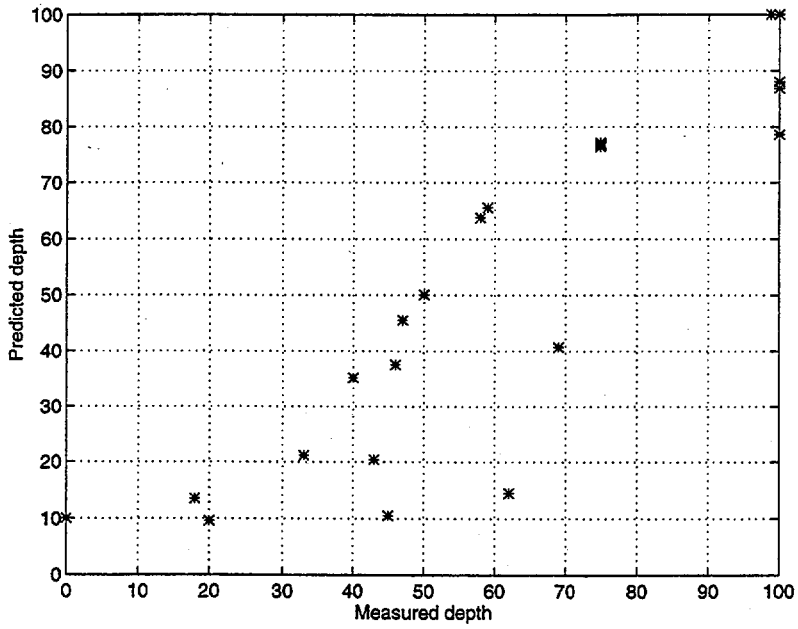

Fig. 3.7. Maximum measured vs. predicted depth in percent of wall thickness for all available specimens when training set consisted of all calibration standard tubes with axial and circumferential indications, plus two specimens with shallow OD indications (used for noise suppression).

3.2 Correlation of Failure Pressure with Bobbin Probe Measurements

Conventional repair and plugging criteria for SG tube integrity are based on estimated degradation depth. Tubes with EC indications that correspond to degradation greater than a specified limit (typically >40% of nominal tube wall thickness) are either repaired (by sleeving) or taken out of service (e.g., plugged). For some types of degradation, e.g., those characterized by short deep crack segments separated by ligaments, depth measurements of an individual crack may not be the best measure of structural integrity. For ODSCC indications at TSP intersections, a voltage-based alternate plugging criterion (APC) has been developed. The criterion is based on direct correlation of bobbin coil voltage amplitude, rather than estimated defect depth, to failure pressure and leak rate. NRC guidance for the application and development of such criteria are provided in Generic Letter 95–05. The correlations between voltage and failure pressure and leak rate have been developed empirically from inspection data and tests on service-degraded pulled-tube specimens and laboratory-grown cracks.

An objective of the SG tube integrity programs at ANL is to assess existing models that correlate NDE results to parameters that are related to tube integrity. As part of this work, the data on pulled and model boiler tube specimens that were originally used by the Westinghouse Owners Group to develop an APC for ODSCC indications at TSP locations in Westinghouse plants that use drilled tube support plates have been reanalyzed by using multivariate regression analysis. Recent work in this area at ANL has focused on examination of

multivariate regression analysis and neural networks to develop empirical models to relate bobbin probe data with tube failure pressures.

Our initial studies on alternate correlation models focused on independent analyses of pulled and laboratory (model boiler) tube test sets. Both MLR and neural-network models were successful in producing reasonable correlations for the individual data sets. Signal features, such as maximum and integrated amplitude, were considered as model parameters. The signal features ultimately selected were the integrated amplitudes at multiple original and mixed frequencies. Preliminary results of this study on pulled-tube data suggested that an optimal (i.e., minimum number of indications for an acceptable correlation) calibration/training set should include representative tubes that describe the range of variation in inspection data that is included from each SG unit. As expected, prediction confidence intervals were narrower for the model boiler test set. Subsequent attempts to develop correlation models with a combined set of pulled and model boiler specimens by using similar EC test parameters failed to produce acceptable prediction confidence intervals. Eventually, an independent normalization procedure was devised for this analysis. Hypothetical test case calibration and prediction scenarios, which utilized a PLS algorithm described earlier in this report, were then implemented to check the stability of the model predictions. It should be noted that the robustness of any correlations developed in this study might be limited by the range of crack morphologies and inspection artifacts included in the available database.

Multiple Linear Regression and Neural-Network Model; ARC Data Base. Current alternate plugging and repair criteria (APC) for ODSCC degradation at TSP intersections for 22.2-mm (0.875-in.)-diameter tubing are based on bobbin voltage amplitude (e.g., signal amplitude from 400/100 kHz mixed frequency channel). Unlike conventional procedures that relate degradation size to tube integrity, the APC is based on direct correlation of tube structural integrity (i.e., failure pressure and leakage) with bobbin voltage amplitude.

The use of multivariate regression analysis procedures and neural-network models to develop the relationships between bobbin probe signals for ODSCC degradation in the TSP area and tube failure pressure have been studied. Forty-one indications from the ARC database were used for the analysis. The indications were from 22 model-boiler and 19 pulled-tubes. All of the examined tubing was 22.2 mm (0.875 in.) in diameter, with a nominal wall thickness of 1.27 mm (0.05 in.). The pulled-tube indications were from the first three TSPs on the hot leg side. The pulled-tube specimens are from three plants. Table 3.7 lists the number of specimens from each SG unit that were incorporated for analysis. Table 3.8 lists the indications from the ARC model-boiler tube database that were included in the analysis. Before a specimen was included in the analysis, the following information about it was required: an ASME calibration standard data file, a measured failure pressure, and data at a consistent set of EC inspection test frequencies (400, 200, 100 absolute and differential channels). Although procedures to correlate EC readings at different test frequencies for similar-type probes have been proposed, to avoid an additional source of uncertainty, such procedures were not used.

Figure 3.8 is a histogram plot of the distribution of measured failure pressure for pulled- and model-boiler-tube indications. As stated earlier, the pulled- and model-boiler tube populations cluster at high and low failure pressures, respectively, with relatively few data points at intermediate pressures. Furthermore, the NDE measurements are affected by such

Table 3.7. Composition of pulled-tube specimens from ARC data base incorporated for failure pressure analysis.

Plant	SG Unit	Indication no.
A	1	1 - 4
A	2	5 - 8
B	1	9 - 11
C	1	12 - 19

Table 3.8. Destructive examination and failure pressure measurements for 22.2-mm (0.875 in.)-diameter tubes from ARC model-boiler database that contained ODSCC degradation at TSP intersections.

Specimen No.	Destructive Examination[a]		Adjusted Pressure[c] (psi)
	Maximum Depth (%)	Length[b] (in.)	
528-2	100	0.67 (0.5)	4,668
532-1	100	0.7 (0.52)	4,010
532-2	100	0.75 (0.58)	4,087
535-1	100	0.28 (0.11)	8,265
555-3	100	0.75 (0.42)	4,209
533-4	100	0.34 (0.14)	6,964
536-1	90	0.4	7,959
542-4	N/A	N/A[d]	>4,867
543-1	N/A	N/A	>2,633
543-2	N/A	N/A	>3,153
543-4	98	0.52	5,459
547-1	N/A	N/A	5,561
576-2	100	0.3 (0.22)	6,628
576-4	100	0.6 (0.43)	5,602
557-1	90	0.18	>7500
557-2	100	0.52 (0.44)	>4,974
557-4	N/A	N/A	11,633
558-1	100	0.4 (0.32)	5,969
568-1	100	0.33 (0.25)	6390
568-2	N/A	N/A	>4,635
571-1	100	0.44 (0.35)	>4,950
574-4	100	0.39 (0.33)	5,506

[a] Measurements were carried out by Westinghouse Electric Corporation.

[b] Total crack network length, with throughwall degradation length given in parentheses.

[c] Normalized to 150 ksi flow stress (sum of yield and ultimate stress).

[d] N/A: Data not available.

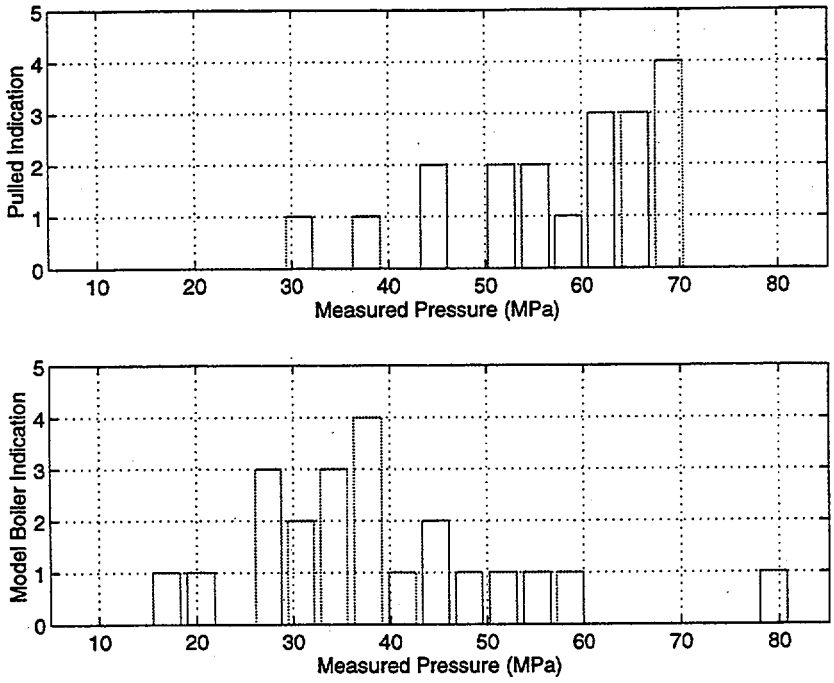

Fig. 3.8. Distribution of pulled-tube (top) and model-boiler (bottom) indications as a function of failure pressure used for multivariate analysis.

factors as variations among calibration standards, probe wear, and dissimilarity of tube/artifact geometry (i.e., NDE carried out with or without TSPs in place, presence or absence of deposits, etc.) as well as actual differences in defect size and morphology.

To reduce the influence of such factors on NDE data, the EC readings were normalized and frequency-mixed. The normalization procedure consisted of automatic phase angle adjustment for each channel and amplitude scaling in reference to four 20% FBHs on an ASME calibration standard tube. For 400/100, 400/200, and 200/100 kHz, where the upper frequency was taken as the primary channel, linear two-frequency least-squares mixes were used to reduce/suppress the TSP signal. A three-frequency 400/200/100 mix was also examined, and, based on the regression analysis results, provided a small improvement over the 400/100 mix. The mixing algorithm was carried out for all data files regardless of whether or not the file contained a TSP indication. The resampled data points for the mixed signals were chosen to cover the entire support plate region.

All manipulations of NDE data, such as searching each file for proper channel configuration, selection of data segments that contain indications at the TSP region, normalization, resampling, and construction of mixed-frequency channels, were implemented by a series of computer codes implemented at ANL as described in Section 2.

The integrated area under each TSP indication was determined by the equation

$$S_f^{A,D} = \sum_{n=-N/2}^{N/2} \left(\left| H_n + i * V_n \right| \right), \tag{3.8}$$

where S represents the integrated signal magnitude at frequency f for each absolute A and differential D channel, and H and V are the horizontal and vertical signal components at each frequency. The integrated region was bounded by $N/2$ points on either side of the TSP center (n = 0), with the sampling rate of each data segment being adjusted in accordance with the simulated TSP ring from the corresponding ASME tube standard.

Although the integrated TSP signal of Eq. 3.8 could be correlated reasonably well with the tube failure pressure when the model-boiler and pulled-tube data sets were considered separately, the correlation when both types of specimens were included in a single database was poor. Consequently, additional transformations of the signals were explored. The selected transformation involved mean-centering and energy-scaling of each data segment independently. Mean-centering is performed to reduce the effect of signal offsets; energy-scaling, to render equal weight for each data segment. As in the case of Eq. 3.8, the integrated area under the transformed signals was determined by

$$\hat{S}_f^{A,D} = \sum_{n=-N/2}^{N/2} \left(\left| \hat{H}_n + i * \hat{V}_n \right| \right), \tag{3.9}$$

where the transformed $\hat{H}$ and $\hat{V}$ components are defined as

$$\hat{X}_n = \left(X_n - \mu^X \right) / \xi^X, \tag{3.10}$$

where μ represents the mean and ξ is the signal energy. For equal-length mean-centered signal component ξ^X is proportional to the standard deviation σ^X of each trace. It should be noted that transformation in accordance with Eq. 3.10 will retain the shape of the original impedance plane trajectory (i.e., a lissajous trace).

Training and prediction schemes were subsequently employed to evaluate the ability of each correlation model to capture all of the useful trends in the data. These are designated as:

All: Information from all (both model-boiler and pulled-tube) indications are used to establish the predictor.

LOOT: Leave-one-out technique (LOOT), i.e., a sampling-with-replacement, where the information from all but one tube is used to establish the predictor. The predictor is then used to predict the failure pressure of the one sample not used for training. The procedure is repeated until a prediction result is obtained for all indications available in the database.

Mixed: Information from half of the randomly selected samples is used to establish the predictor, which is then used to estimate the failure pressures of the remaining half.

Initially, all of the available original- and mixed-channel signals (14 components) were incorporated for multivariate analysis to determine the best fit to the data as well as to identify

the minimum number of independent variables that best describe all of the variations in the data.

Figures 3.9a and b display the multivariate regression and the neural-network fits, respectively, when all samples were incorporated for the model-building stage. Also shown are the upper and lower bounds of the 95% confidence interval, calculated through a first order least-squares fit to the measured-vs.-predicted pressure. As expected, the neural-network can better capture all of the variations in the data. However, it should be noted that this test case does not represent the prediction capability of the model but rather the ability of the model to construct a fit to all of the data. Figure 3.10 displays the prediction results of the two models when ≈50% of the indications from each tube category were included in the training stage. For this test case, comparable confidence intervals were achieved by both methods. Finally, Fig. 3.11 displays the prediction results of the two models, based on the LOOT training and prediction scheme. Once more, the confidence intervals for both methods of fitting show comparable prediction accuracy.

Figure 3.12 is a plot of residual vs. regression-predicted failure pressure when all model-boiler and pulled-tube specimens were included in the training. The distribution of residual pressure does not display any distinct pattern, a finding that is consistent with the assumption that a normal distribution of residual pressures is implicit in the calculation of the confidence interval. Figure 3.13 shows the changes in residual failure pressures when the LOOT training and prediction procedure was performed. For multivariate models, the variation of residual pressure obtained with the LOOT procedure is an indicator of model stability. For a stable model, the predictions should be relatively independent of individual data points in the training set, i.e., the residual pressures in Fig. 3.12 should be small when compared with the predicted failure pressures. In the present case, the change in the residuals is ≈10%. For this type of data, such a change is reasonably small.

Figure 3.14a shows a plot of the cumulative distribution of the residual pressure, assuming that it is are normally distributed when the training set included all of the available indications. Figure 3.14b shows similar results when a LOOT training/prediction procedure was implemented. The standard deviation of the distribution when the LOOT procedure was followed is ≈50% greater than when all of the data were used to fit the model. It is possible that the LOOT training scheme provides the most conservative estimate of the accuracy of the predictors.

A study was also carried out to indirectly assess the prediction accuracy of the multivariate regression model by comparing the results presented above with those obtained by using a linear regression model. The data set used in this work consisted of renormalized EC inspection results that were used to develop the voltage-based APC model. One data point from the model boiler set was not used for this analysis because the voltage reading for that indication (i.e., marked as not reliable in the ARC data base) was not available. The renormalization was performed by referencing all measurements to a single ASME tube standard. A linear least-squares fit to the logarithm ($\log_{10}$) of the measured voltage-vs.-failure pressure was implemented in accordance with the APC-recommended model. Although a direct analogy between the APC linear regression and multivariate models cannot readily be described, comparison of the predicted residual pressures suggests tighter global prediction for the multivariate model.

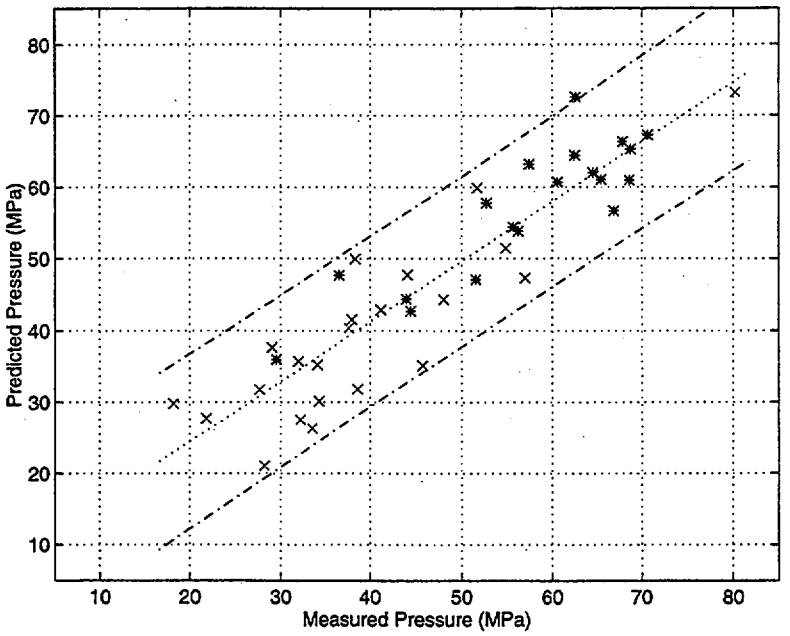

(a)

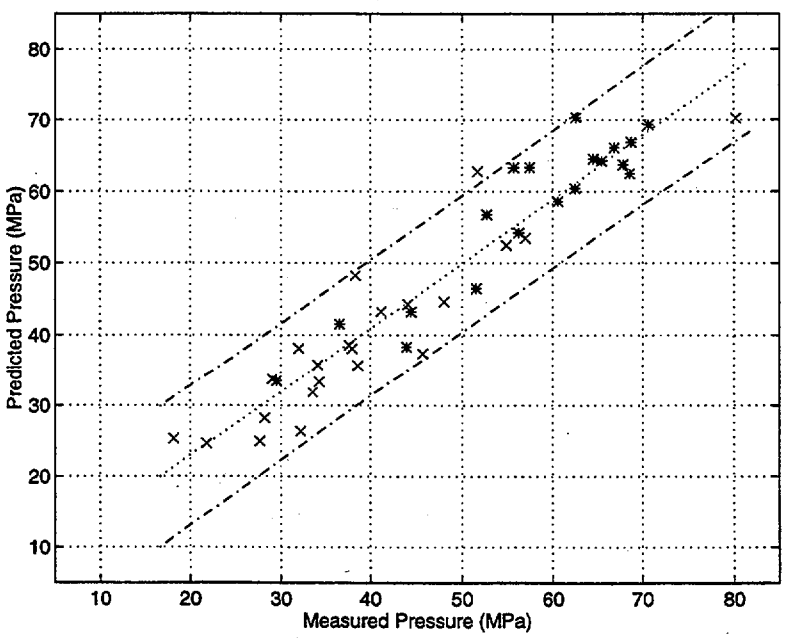

(b)

Fig. 3.9. (a) Regression- and (b) neural-network-predicted vs. measured failure pressure when all model-boiler (x) and pulled-tube (*) indications were included for training. Also shown are the upper and lower bounds of the 95% confidence interval, based on a linear least-squares fit to the data.

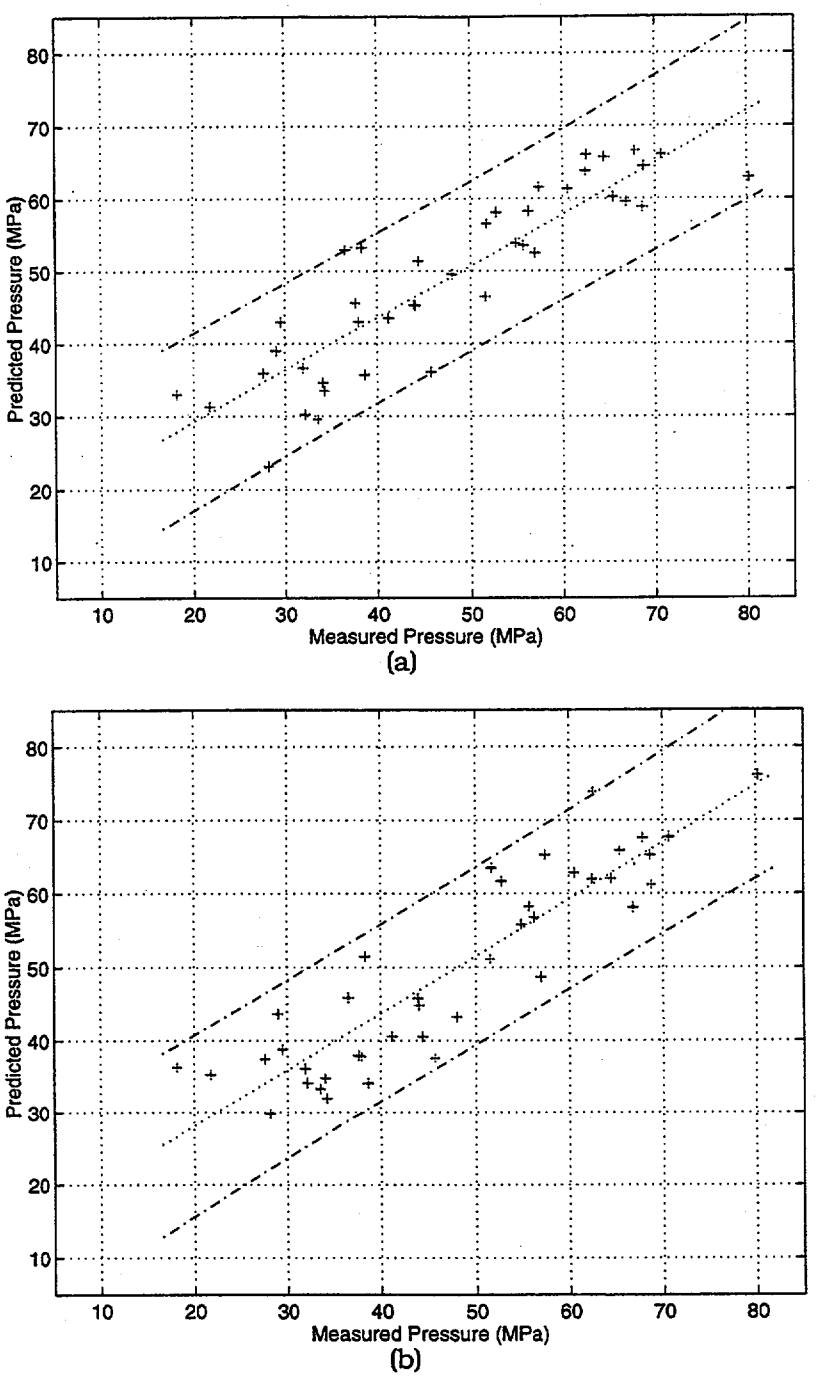

Fig. 3.10. (a) Regression- and (b) neural-network-predicted vs. measured failure pressure when ≈50% of model-boiler and pulled-tube indications were randomly selected for training. Also shown are the upper and lower bounds of the 95% confidence interval, based on a linear least-squares fit to the data.

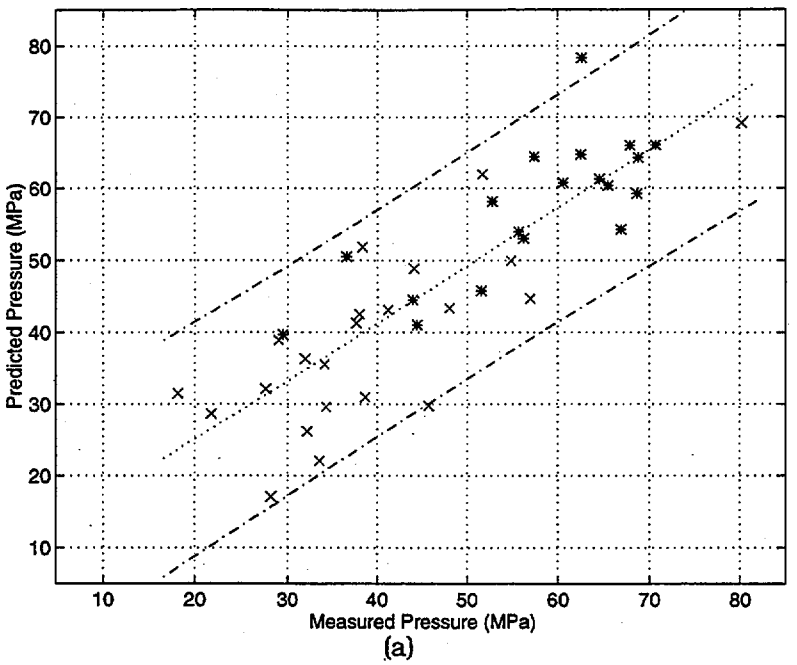

Fig. 3.11. (a) Regression- and (b) neural-network-predicted vs. measured failure pressure for model-boiler (x) and pulled-tube (*) indications, with LOOT training and prediction method. Also shown are the upper and lower bounds of the 95% confidence interval based on a linear least-squares fit to the data.

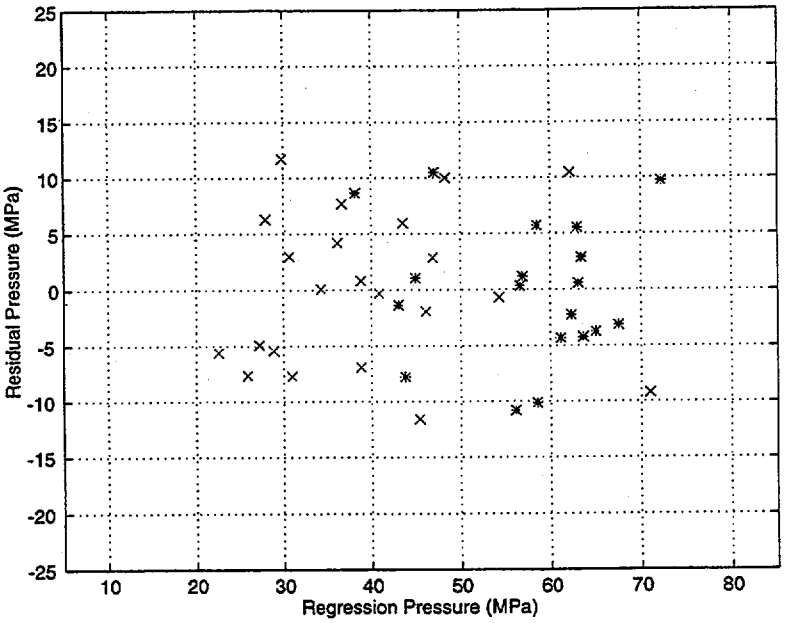

Fig. 3.12. Residual vs. regression-predicted failure pressure when all model-boiler (x) and pulled-tube (*) specimens were included for training.

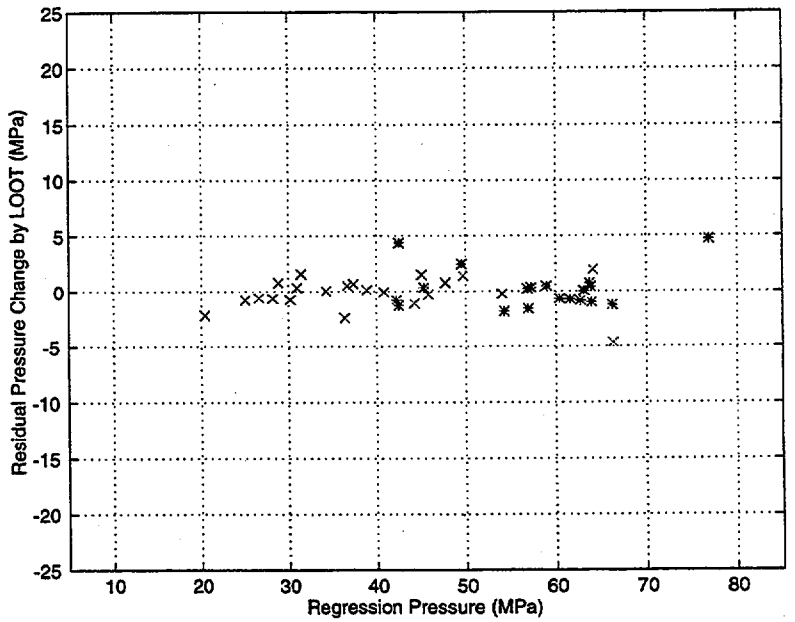

Fig. 3.13. Change in predicted residual failure pressure shown in Fig. 3.12 for model-boiler (x) and pulled-tube (*) specimens when a LOOT training and prediction scheme was followed.

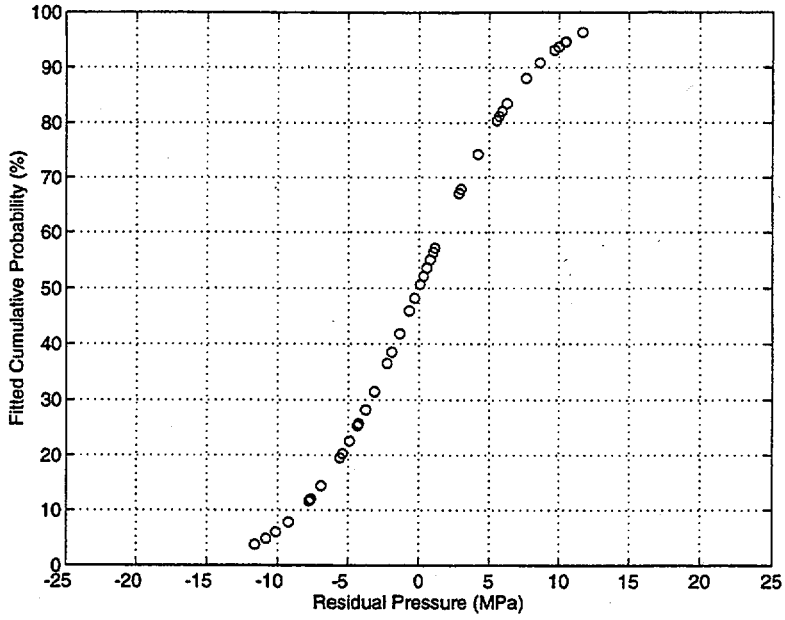

Fig. 3.14. Cumulative distribution of residual failure pressure, based on an assumed normal distribution function, with training and prediction based on (a) all indications, and, (b) LOOT.

The failure pressures predicted by the APC linear regression model vs. measured failure pressures are shown in Fig. 3.15. Also shown is the 95% confidence interval for the first order least-squares fit of the measured-vs.-predicted failure pressures. A linear correlation coefficient R of ≈0.88 was calculated for this fit. Figure 3.16 is a plot of the residual failure pressure vs. regression-predicted pressures. Once again, the distribution of the residual pressures does not display any distinct pattern, a finding that is consistent with the assumption that a normal distribution of residuals is implicit in the calculation of the confidence interval. Assuming that the residual failure pressure is normally distributed, the comulative distribution of the residual pressure is shown in Fig. 3.17.

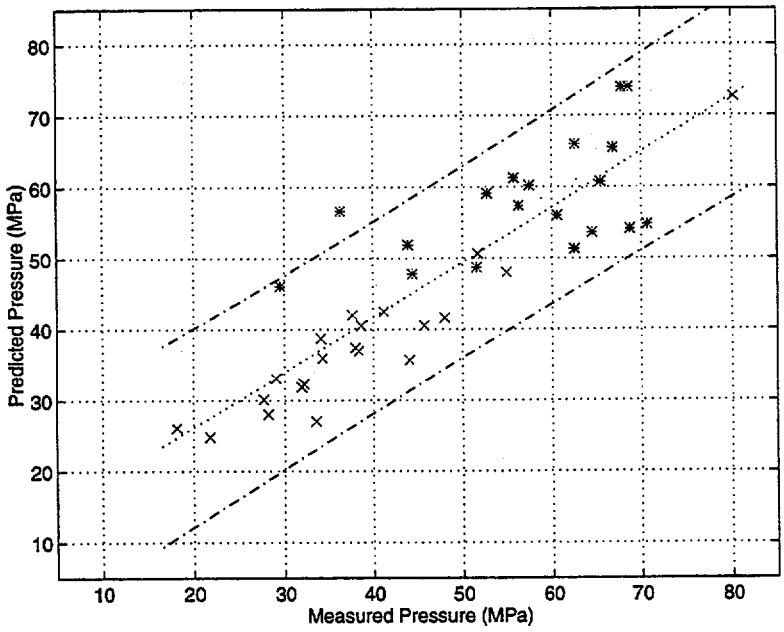

Fig. 3.15. Regression-predicted vs. measured failure pressure for all model-boiler (x) and pulled-tube (*) indications, using the APC model. Also shown are the upper and lower bounds of the 95% confidence interval based on a linear least-squares fit to the data.

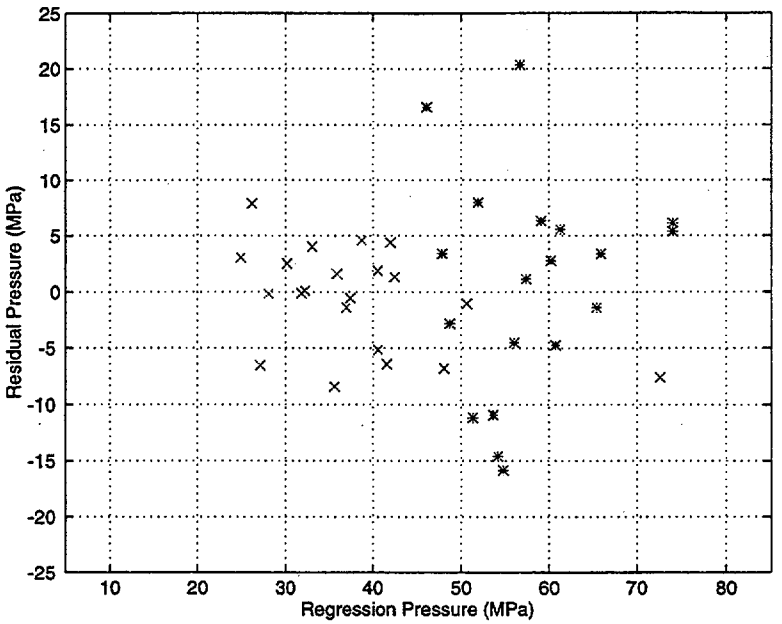

Fig. 3.16. Residual vs. regression-predicted failure pressure for all model-boiler (x) and pulled-tube (*) specimens, using the APC model.

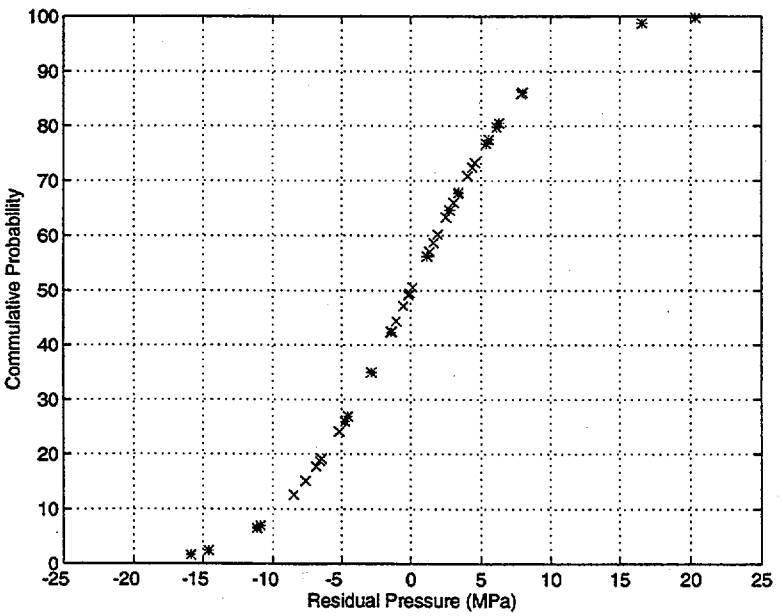

Fig. 3.17. Cumulative distribution of APC model residual failure pressure, based on an assumed normal distribution function.

4 Advanced Ultrasonic NDE of Steam Generator Tubing

4.1 Guided Ultrasonic Waves

Guided waves (Lamb waves) were explored as a possible method to help characterize defects in SG tubes and to help identify attributes that may be useful for characterizing defects during field inspections. One significant advantage of Lamb waves is their insensitivity to the presence of roll transitions. This insensitivity makes it easier to detect cracks at the transition of rolled tubes. In addition, Lamb waves will be less sensitive to the presence of artifacts such as support plates and deposits and can be used to detect flaws at a distance.

The Lamb wave inspections were carried out from the inside of the tube, with the tube filled with water and the contoured plastic wedge of the probe in contact with the tube ID surface. A specially fabricated Lamb wave probe with a 6-mm piezoelectric crystal on a wedge (Fig. 4.1), operating in a pulse echo mode, was used. Figure 4.2 shows the echo from a circumferential ODSCC in an Alloy 600, 22.2-mm (7/8-in.)-diameter tube with a laboratory-grown crack in the transition region of a tube that had been mechanically rolled into a heavy metal collar to simulate the geometry at the top of the tube sheet. Ultrasonic diffraction and EC evaluation of the crack suggest that its maximum depth is 80% throughwall. With the probe on the inside of the tube and 75 mm from the crack, the Lamb wave echo is clearly evident. The crack is ≈140° in circumferential extent. With the probe on the side of the tube opposite from the crack, only a relatively weak signal from the roll transition is evident.

In general, the attenuation of Lamb waves is relatively low attenuation and echoes from defects in the tube wall can, in principle, be obtained for long distances between probe and defect. In our tests, the amplitude of the echo varied only moderately as the probe was moved along the axis, thus, by moving the probe a measured distance and noting the change in transit time of the echo, the Lamb wave velocity can be measured. A value of 4800 m/s was measured for an ultrasonic frequency of 1.2 MHz. Rose et al.[3] measured a velocity of 4790 m/s and theoretically derived a L(0,2) mode group velocity of 4670 m/s at 1.2 MHz and a wall thickness of 1.25 mm. Rose et al. also noted that the frequency of 1.2 MHz was especially effective for water-filled tubes, a finding that is consistent with the present results.

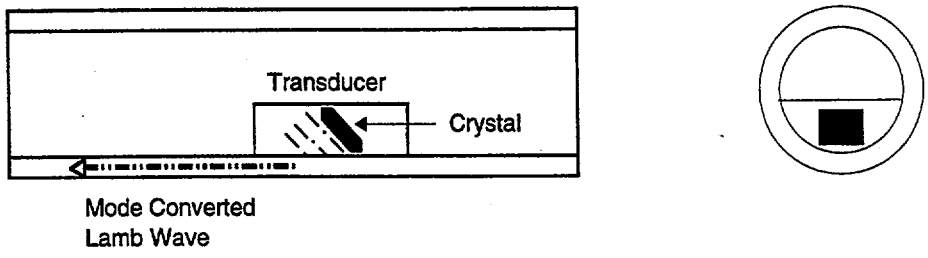

Fig. 4.1. Specially fabricated Lamb wave probe with 6-mm piezoelectric crystal on a wedge, operating in pulse echo mode.

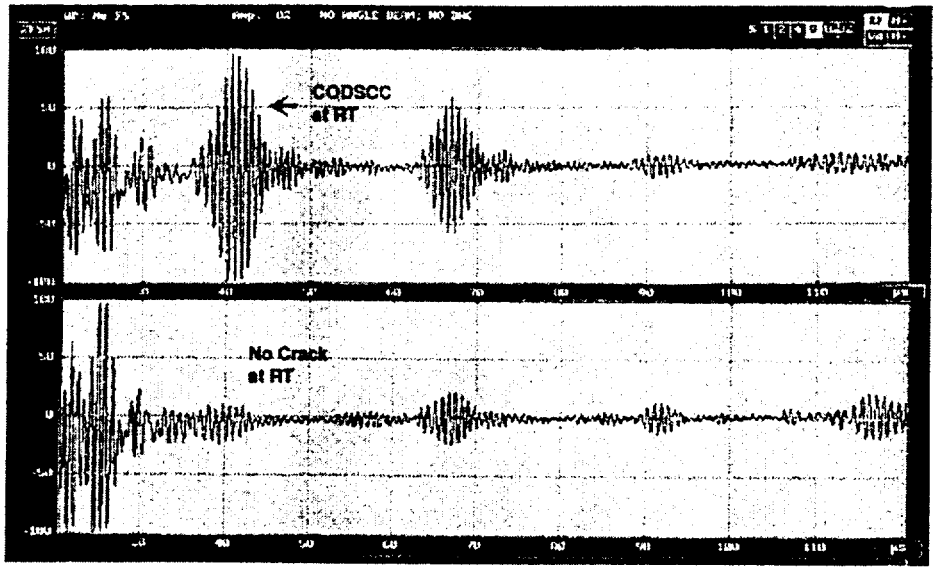

Fig. 4.2. Ultrasonic Lamb wave echo (top half of figure) from a circumferential ODSCC in an Alloy 600, 22.2-mm (7/8-in.)-diameter tube with a laboratory-grown crack in the roll transition. UT and EC evaluation suggest a maximum depth of 80% throughwall.

Attenuation measurements were made on Alloy 600, 22.2-mm (7/8-in.)-diameter tubing filled with water. For a transducer-to-end-of-tube distance of 10-50 cm, the echo amplitude of the signal at 1.2 MHz decreased by ≈12 dB and then remained approximately constant (with S/N ratio of ≈5:1) up to a maximum distance of 250 cm.

The variation of the amplitude of the reflected wave with crack depth was also studied. Figure 4.3 shows the results for circumferential OD EDM notches, laser cut slots, fatigue cracks, and a circumferetial ODSCC for a 40-μs acoustic path (≈75-mm wedge-to-crack distance). The depth of the circumferetial ODSCC is estimated from other ultrasonic and EC measurements. All of the reflectors are wider than the transducer crystal. Depth estimates determined by other means, such as crack tip diffraction, are generally accurate for notches and fatigue cracks.[1] Figure 4.4 shows measurements for a 60-μs round trip time for the echo. No relationship between signal amplitude and depth is evident for the 60-μs path, although a slight monotonically increasing trend is seen for the shorter 40-μs acoustic path.

Although these results show that the amplitudes of the Lamb wave echoes are not very sensitive to depth, the amplitude gives some estimate of the depth when the probe is close to the defect. Better estimates of depth might be obtained by comparing, simultaneously, the echo amplitude of two Lamb wave modes; however, a unique and specialized probe would be required to make that kind of measurement.

Lamb waves may be most useful in the detection of circumferential cracks in the roll transition and in the determination of the length of such cracks. They can be used to image the circumferential extent and segmentation of such circumferential cracks. Because they can provide detectable signals over relatively long distances, Lamb wave probes could be used to

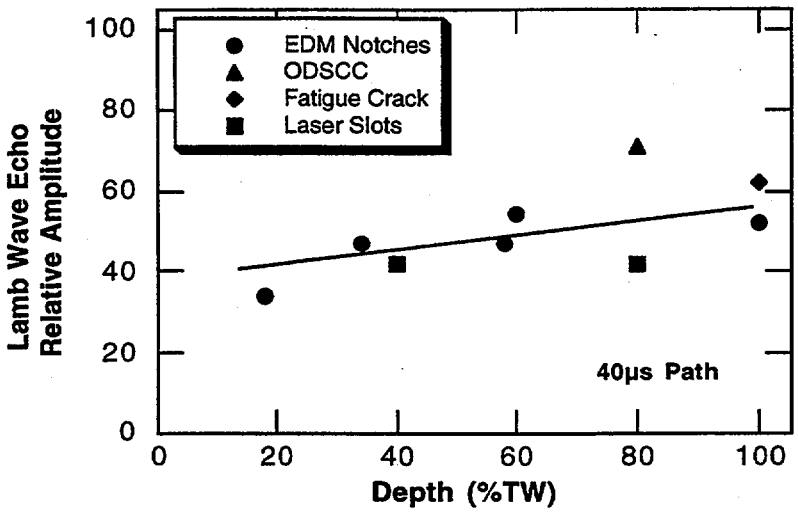

Fig. 4.3. Dependence of ultrasonic Lamb wave amplitude on crack depth, evaluated with numerous tubes and 40-µs round trip transit time.

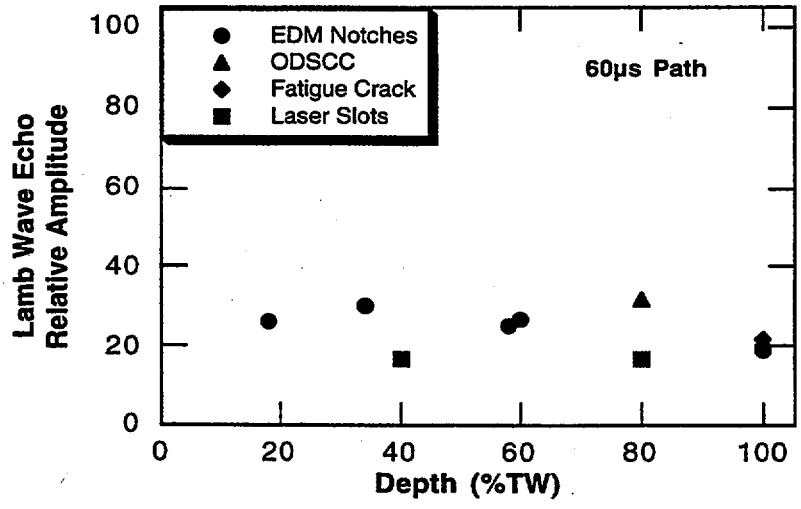

Fig. 4.4. Dependence of Lamb wave amplitude on crack depth, evaluated with numerous tubes. Measurements are reported for Lamb wave probe with 60-µs round trip times for the echoes.

examine the tube sheet without having to insert the probe very far. Time-of-flight measurements of flaw echoes could be used to determine the axial position of a defect. Although axial cracks are not detectable with the probes that have been used for the current studies unless circumferentially oriented branches are present, it is possible, in principle, to make a Lamb wave probe that could detect axial cracks.

Using a Lamb wave probe, M. Brook at ABB-AMDATA examined SG tube samples with circumferential SCC. Calibrations for these examinations were carried out with a standard that contained circumferential EDM notches with throughwall depths of 20, 40, and 60% and arc lengths of 20, 40, and 60°. The signal from a 20% TW, 60° arc notch was set to 80% full screen height. The probe was moved axially 1.3 mm (0.05 in.) for every 360° scan. A-, B-, and C-scans were generated. The scan mode covered a range of 140 mm (5.5 in.). The probe was operated at a frequency of ≈5 MHz. A PC-based Intraspect ultrasonic system was used to collect the data. As indicated previously, not enough information is present in the Lamb wave echo signal to determine the depth, but general estimates can be made by measuring the echo amplitude. The length of the defect is accurately estimated by observing the drop in signal amplitude as the defect is scanned.

The image obtained from a laboratory-grown circumferential ODSCC in the roll transition of a 22.2-mm (7/8-in.)-diameter Alloy 600 tube section is shown in Fig. 4.5. The horizontal axis represents the full circumference of the tube. The segmentation and relative axial positions of the segments are clearly seen. There appear to be six crack segments, with five at the same axial location and one offset axially with an arc length of 50°. The total arc length indicated by UT is 130°. Destructive analysis (by PNNL) showed a crack with a total arc length of 160°, with a segment showing an arc length of 60° axially offset from the larger segment by ≈1.3 mm (0.05 in.). Although destructive examination of the lower part of the crack shown in Fig. 4.5 does not reveal well-defined segments, it does show widely varying depths for this portion of the crack. The segments indicated ultrasonically are presumably the result of low-amplitude signals from the shallow parts of the continuous crack.

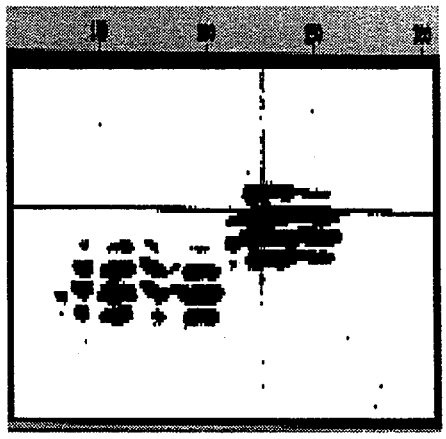

Fig. 4.5. Ultrasonic Lamb wave image (from ABB-AMDATA) of laboratory-grown circumferential ODSCC in an Alloy 600 SG tube.

4.2 Acoustic Microscopy

In collaboration with Sonoscan Inc. (Bensenville, IL), high-frequency ultrasonic imaging has been explored as a possible method to help characterize defects in SG tubes. Although intended primarily for laboratory investigation, acoustic microscopy could be applied in the field in special cases.

In this approach, ultrasonic waves with frequencies of ≈50 MHz are used to generate a crack shadow. The measurement of depth is determined directly from the extent of the ultrasonic shadow on the OD of the tube. The part of the beam that misses the crack passes through the tube wall and is scanned and imaged by a 50-μm spot-size receiving transducer oriented to receive the ultrasonic wave as it passes through the tube wall. All coupling is accomplished with water. Figure 4.6 shows a schematic representation of the acoustic microscope.

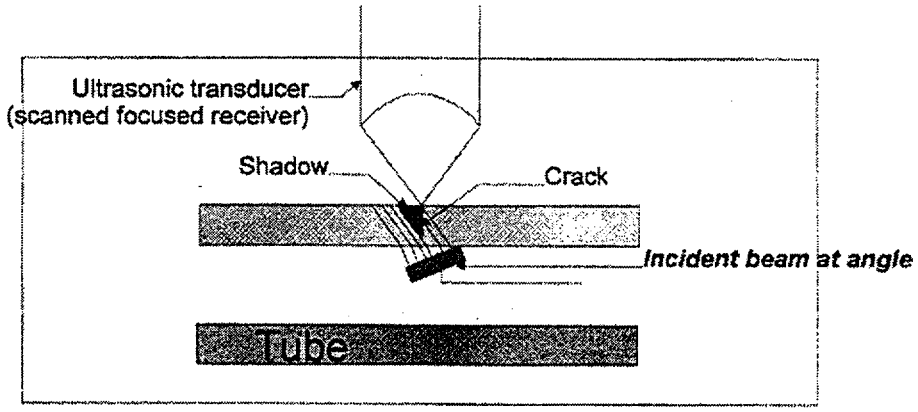

Fig. 4.6. Schematic representation of the Sonoscan Inc. acoustic microscope. 50-MHz ultrasonic waves, launched from inside the tube, were received by a focused transducer at the tube OD. A special fixture is used to hold the transducer at the correct angle of incidence to launch a 50-MHz, 45° longitudinal beam from the ID.

The shadow of a 60% TW laser cut slot was examined. A special fixture was used to hold the transducer at the correct angle of incidence to launch a 50-MHz, 45° longitudinal beam from the ID. Figure 4.7 shows the acoustic shadow of a laser-cut slot. The beginning and end of the shadow are clearly evident. Because through-transmission waves are used, this configuration could not be used under field conditions. A pulse echo mode configuration with transmitter and receiver on the ID would have to be used for field work.

Several other tubes were also examined. Excellent results were obtained from laser-cut slots and from EDM notches. The estimated-vs.-actual depth for two notches, using 50-MHz ultrasonic waves, is shown in Fig. 4.8. A throughwall fatigue crack in an Inconel 600 SG tube was also examined. This crack, which initiated on the OD, could be profiled over a depth range of 100% TW to ≈40% TW. However, SCCs, which are typically very tight, do not appear to produce shadows as clear as those produced by notches or fatigue cracks. Because the tip is

the tightest portion of the crack, crack depths would be expected to be underestimated. An example from a tube with an ODSCC is presented in Fig. 4.9. From the shadow in this figure, the estimated depth is ≈10% TW. Based on estimates from +Point data, which have been shown to be reasonably accurate for cracks of this type by destructive evaluation, the depth is more likely to be ≈25% TW. The difficulties in estimating depths of SCCs by acoustic microscopy suggest that significant difficulties could also be encountered with procedures that attempt to use crack-tip echoes to estimate depth (from time-of-flight differences between tip echo and bottom-of-crack echo). Cracks that cannot be shadowed also will not scatter significant ultrasonic energy to reveal the location of the crack tip and thus lead to underestimates of the depth.

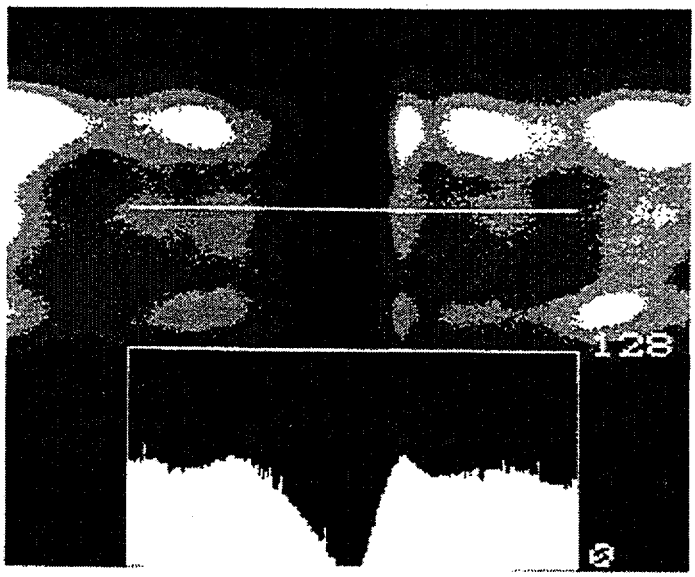

Fig. 4.7. Ultrasonic shadow of a 60% TW laser-cut slot produced by an angled 50-MHz shear wave launched from inside a water-filled tube, which is horizontal in the photograph. Tube axis is represented by the white line. A highly focused (50-μm spot size) water-coupled receiving transducer was used to scan the outer surface of the tube to create the shadow from the through-transmitted ultrasonic waves. Black band is the shadow of the laser-cut slot. Figure below the shadow shows amplitude as a function of position in the shadow along the white line. (Image courtesy of Sonoscan Inc.)

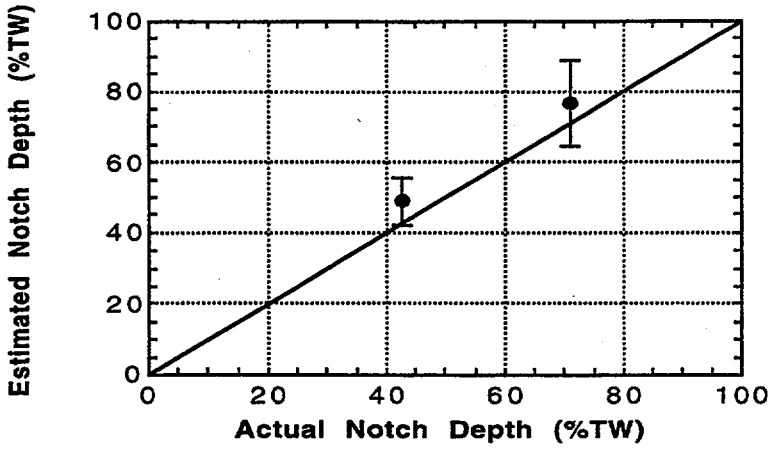

Fig. 4.8. Depth estimated by acoustic microscopy vs. actual depth of two EDM notches in two Alloy 600 22.2-mm (7/8-in.)-diameter tubes.

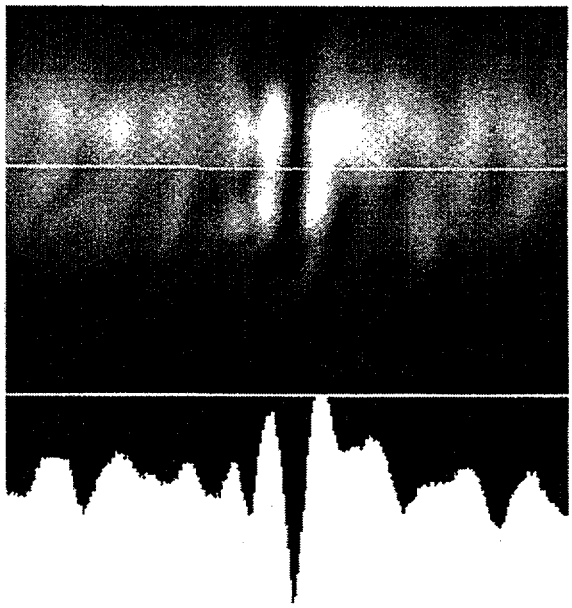

--> <-- Width of ultrasonic shadow is used to estimate crack depth

Fig. 4.9. Shadow of crack from tube with ODSCC. From this shadow, estimated depth is ≈10% TW. Depth is estimated from extent of shadow on OD of the tube.

4.3 Laser-Cut Slots for Calibration and Modeling

Laser-cut slots in 22.2-mm (7/8-in.)-diameter Alloy 600 tubes for calibration and model validation have been prepared by Oxford Lasers, Ltd. Figure 4.10 is a photomicrograph of a representative axial OD laser-cut slot (Oxford Laser Ltd.), 75% TW (0.95 mm), in an Alloy 600, 22.2-mm (7/8-in.)-diameter tube. Sectioning of this slot revealed occasional bridging across the faces, as expected. The opening at the OD was ≈50 μm.

Although laser-cut slots are somewhat more representative of field cracks than an EDM notch because they are tighter, they may not be a good choice for a calibration standard because the possibility of bridging across the slot faces may make it difficult to obtain reproducible results for EC data calibration. The potential difficulty can be illustrated by comparing the EC responses to 40 and 80% throughwall circumferential OD laser-cut slots that are 25.4 mm (1 in.) long.

Eddy current signal amplitudes from 40 and 80% TW EDM notches that were measured with a +Point™ probe differ by about a factor of three. The corresponding amplitude from the 80% TW laser-cut slot was only ≈30% higher than that from the 40% TW slot. Phase angle analysis with a +Point™ probe at 200 and 400 kHz, based on calibration on circumferential OD EDM notches, gave estimated depths of 50-60% for the 80% TW laser-cut slot and ≈20% for the 40% TW laser-cut slot.

Laser-cut slots may be useful for assessing depth estimation techniques because their maximum depths are known with reasonably high confidence. Laser-cut slots could also be used for modeling to validate predicted EC response to features such as ligaments or bridging across crack faces.

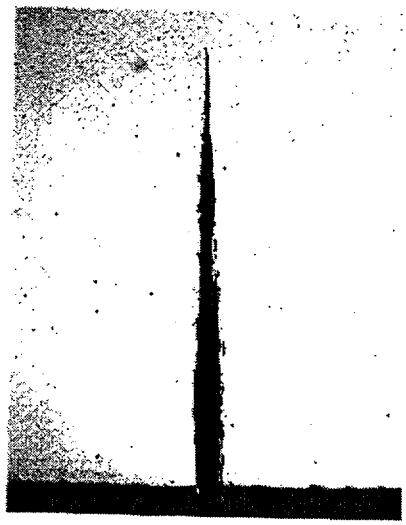

Fig. 4.10. Photomicrograph of axial OD laser-cut slot (Oxford Laser Ltd.), 75% TW (0.95 mm), in Alloy 600, 22.2-mm (0.875-in.)-diameter tube. Sectioning of slot revealed occasional bridging across the faces, as expected from this process. Opening at OD is ≈50 μm.

4.4 Bore-Side Ultrasonic Examination of Tubes with Electrosleeve™ Repairs

The Electrosleeve™ is a method of repairing SG tubes that uses a sleeve of ultrafine-grained nickel electrochemically deposited on the inner surface of a degraded tube to form a structural repair. The thickness of the Electrosleeve™ is ≈1-mm, comparable to the 1.3-mm wall thickness of the parent tube. The use of EC and ultrasonic techniques for NDE of tubes with Electrosleeves™ has been carried out at ANL.

The ultrasonic techniques for detecting circumferential and axial cracks that were investigated involved the use of probes that were sized for the opening and curvature of a 22.2-mm (7/8-in.)-diameter tube with an Electrosleeve™ repair. One circumferential probe, operating at 5 MHz, launches 45° shear waves in a pulse echo mode from the tube ID with either water or glycerol as couplant. A second probe launches 70° shear waves. Both probes can detect a 13-mm-long, 0.5-mm-deep (40% TW) OD circumferential EDM notch in the parent tube.

A third compound probe launches 45 and 70° waves that travel around the tube to detect axially oriented flaws. This compound probe can detect a 0.5-mm-deep (40% TW) OD axial EDM notch in the parent tube. The signals from the 45° beams are generally stronger than those from 70° beam, as expected. However, the 70° beam may be more effective in detecting planar flaws that do not intersect either the ID or OD of the tube and thus do not exhibit a corner trap reflector. The use of 5 MHz, rather than higher frequencies, helps minimize signal distortion due to the greater surface roughness of the Electrosleeve™. Although these ultrasonic techniques were successful in detecting notches, echoes from SCCs are expected to be considerably weaker than echoes from notches because of the tightness of the cracks. EDM notches may help to establish the limiting case for detection (i.e., SCCs would have to be larger than the smallest detectable EDM notch). Additional tests are planned on tubes with laboratory-grown SCCs.

Eddy current traces obtained with a +Point™ probe at 100 and 300 kHz for the EDM notch samples are shown in Figs. 4.11-4.14, along with the corresponding ultrasonic echo patterns. Because the high conductivity of nickel would reduce the penetration depth of the EC probe, it is somewhat surprising that at 300 kHz, EC signals from notches were detectable. However, the conductivity of the Electrosleeve™ material is lower than that of conventional nickel because of the much smaller grain size and the phosphorus additions. To ensure that the apparent notch signal was not an experimental artifact, a test was performed to verify that a copper foil (20 x 5 x 1 mm) placed on the outside of a flaw-free tube with an Electrosleeve™ could be detected at 300 kHz. Figure 4.11 shows the results for a 1-mm-deep (80% TW) OD circumferential notch in the parent tube. Both the EC and ultrasonic (70° shear) signals are strong and clear. Figure 4.12 shows the results for a 0.5-mm-deep (40% TW) OD circumferential notch in the parent tube. Both the EC and the ultrasonic (70° shear) flaw signals are clear. Figure 4.13 shows the results for a 1-mm-deep (80% TW) OD axial notch in the parent tube. Both the EC and the ultrasonic (70° shear) flaw signals are clear, although the ultrasonic signal exhibits a better S/N ratio. Figure 4.14 shows the results for a 0.5-mm-deep (40% TW) OD axial notch in the parent tube. Both the EC and the ultrasonic (70° shear) flaw signals are detectable, but again, the ultrasonic signal shows a significantly better S/N ratio. Signal-to-noise ratios for axial notches are even better for 45° than for 70° shear waves.

It is more difficult to detect defects that originate on the ID of the parent tube that are not 100% TW, because nonthroughwall cracks do not intersect the OD of the parent tube to form a strong ultrasonic reflector (corner trap). Higher angle beam ultrasonic NDE, including use of surface waves, should be explored for detection of such cracks. The possibility that variations in Electrosleeve™ acoustic properties that could distort the ultrasonic beam and thus lead to missed defects or false calls should also be evaluated.

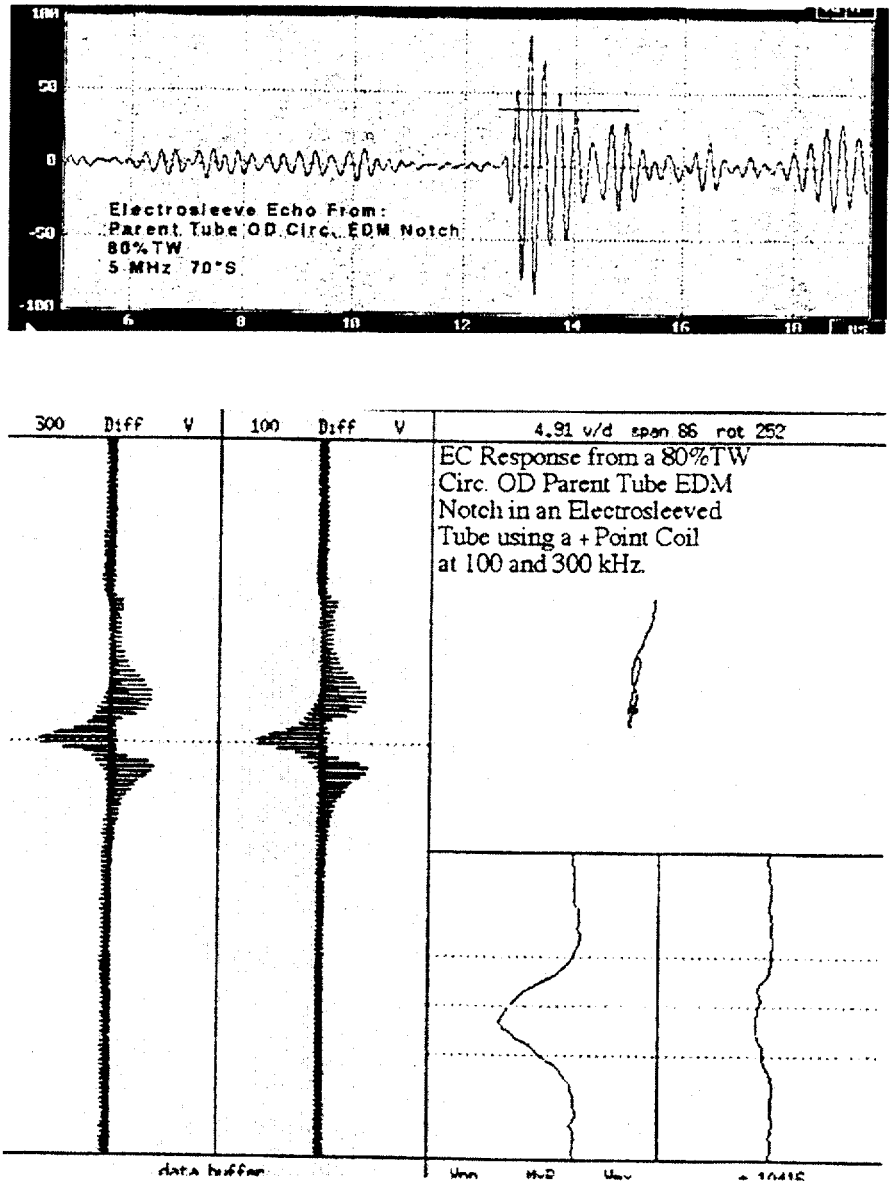

Fig. 4.11. Ultrasonic (top) and EC (bottom) signals from a 1-mm-deep (80% TW) OD circumferential notch in parent metal of Electrosleeved tube. Ultrasonic (70° shear) and EC flaw signals are both strong and clear.

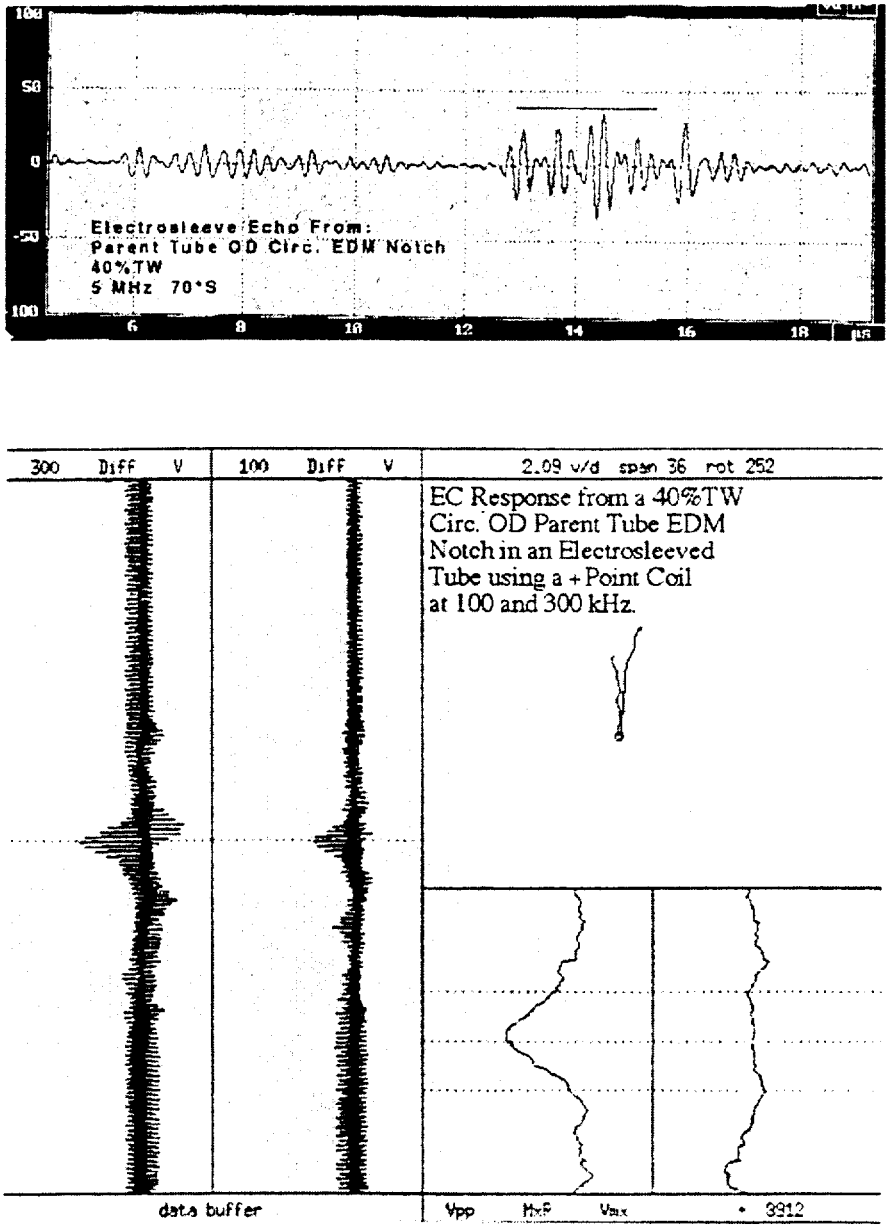

Fig. 4.12. Ultrasonic (top) and EC (bottom) signals from a 0.5-mm-deep (40% TW) OD circumferential notch in parent metal of Electrosleeved tube. Ultrasonic (70° shear) and EC flaw signals are both clear.

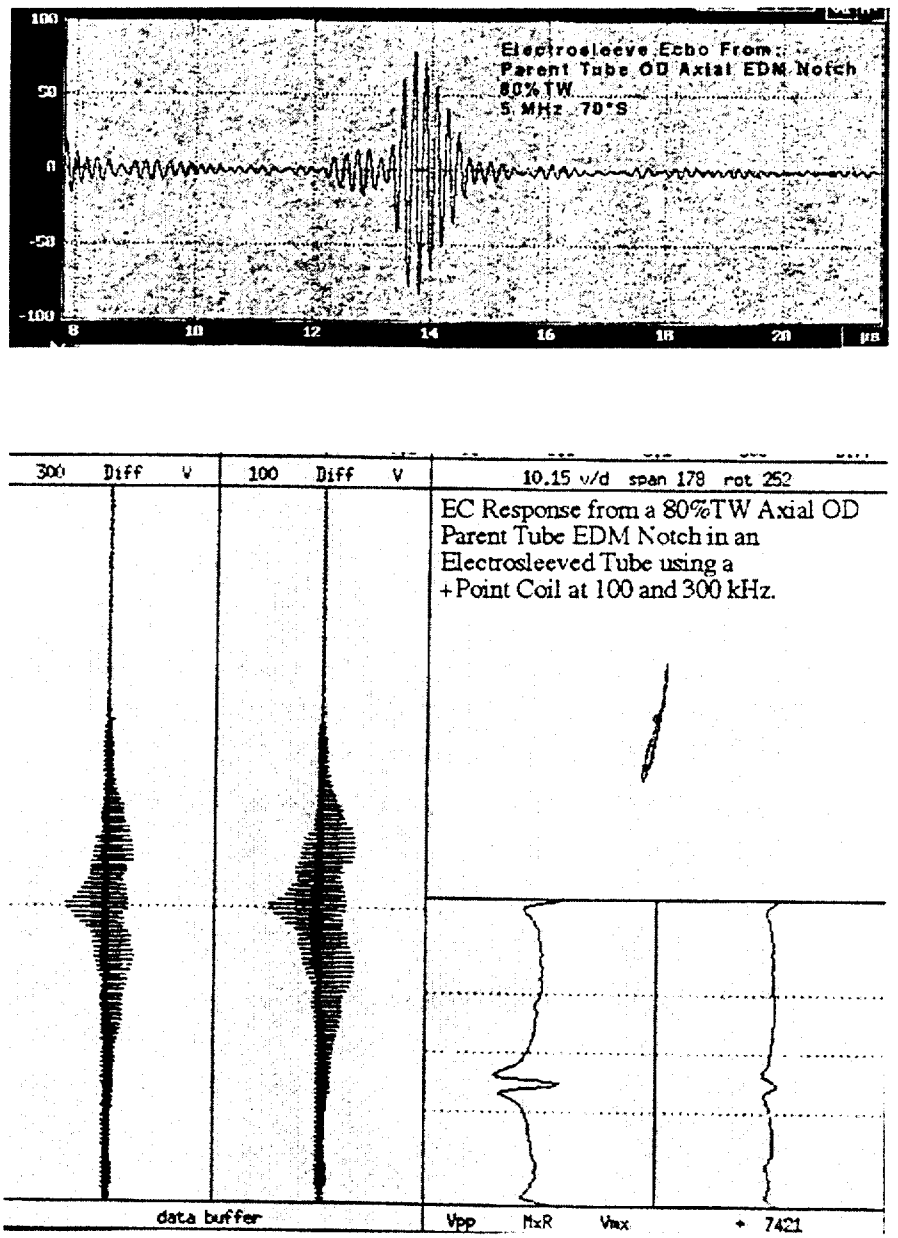

Fig. 4.13. Ultrasonic (top) and EC (bottom) signals from a 1-mm-deep (80% TW) OD axial notch in parent metal of an Electrosleeved tube. Ultrasonic (70° shear) and EC flaw signals are both clear.

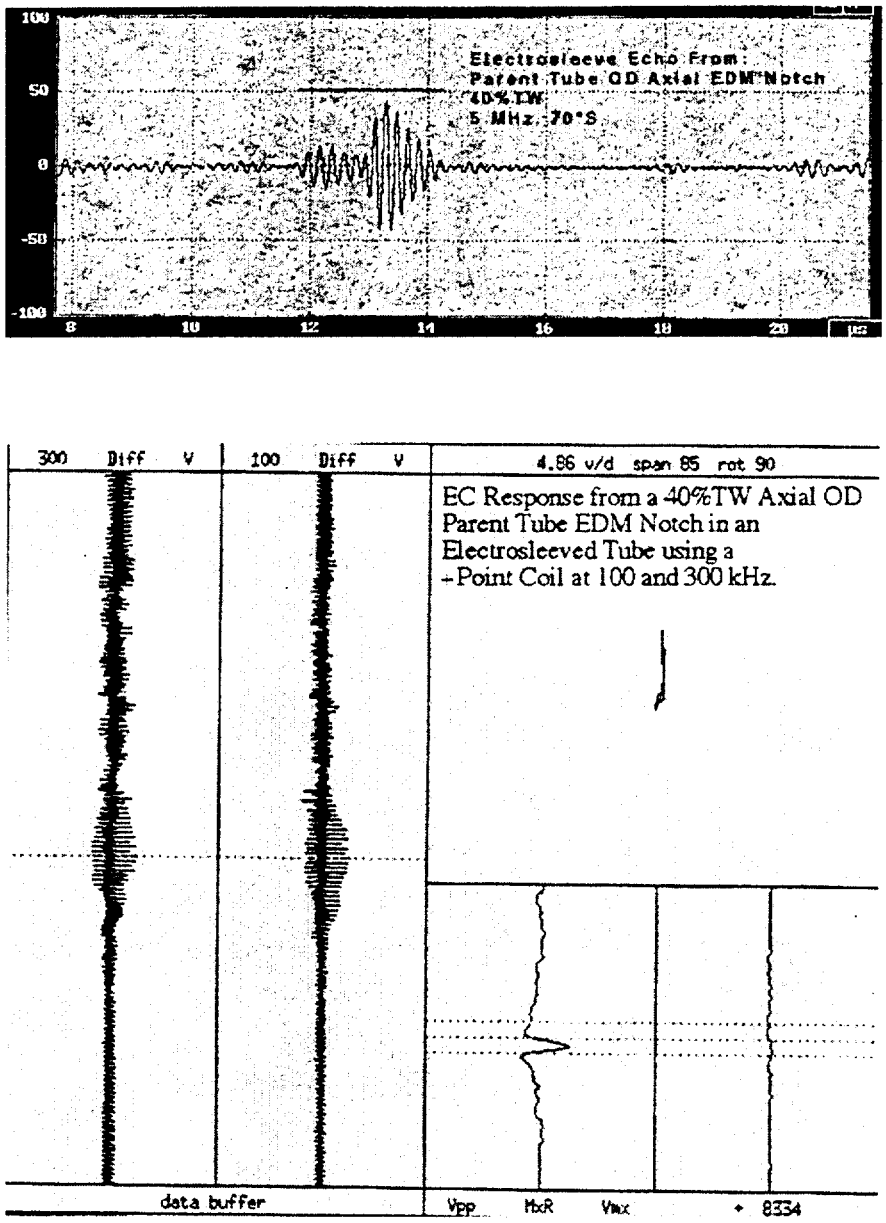

Fig. 4.14. Ultrasonic (top) and EC (bottom) signals from a 0.5-mm-deep (40% TW) OD axial notch in the parent metal of Electrosleeved tube. Ultrasonic (70° shear) and EC flaw signals are both detectable but ultrasonic signal is better.

5 Emerging Technology

The use of fiber optic and satellite links makes possible faster EC data analysis. Raw EC data files can be transferred from an optical disc at a data acquisition location to the data analysis location via a fiber optic or satellite link, thus eliminating a delay of ≈4 h that would otherwise be experienced because of the need to physically transfer the optical disc to an off-site location for analysis. To use digital satellite communication, a transportable earth satellite station can be installed at a plant site, while a permanent earth station can be established at the location where the analysis will take place. Cost savings and faster inspections can be realized with this communication option.[4]

Remote-field EC (RFEC) inspection employs low-frequency alternate current to inspect tubes from the inside. RFEC is a throughwall inspection technique wherein a solenoid coil generates the EC, while detectors are axially displaced from the exciter by two or more tube diameters and may be oriented to measure any component of the flux density. The tube acts as a waveguide; the pickup coil senses mainly the indirect electromagnetic coupling.

In contrast to conventional EC inspection systems, in RFEC inspection, the field on the outside of the tube wall is much greater than the field on the inside. As in conventional EC analysis, defects cause changes in the amplitude and phase of the signal. Impedance plane diagrams are used for signal analysis. In general, the angle of the defect trace on the monitor is used to characterize an anomaly, but amplitude is also used. Unlike the conventional impedance plane, the RFEC voltage plane is not restricted to the first quadrant. Points on the RFEC plot represent amplitude and phase of through-transmission signals. RFEC signals cause almost no phase change and are well separated from lift-off, but separation of various types of defects is relatively difficult. The technique might be useful for characterizing outer-surface defects.[5]

Eddy current analysis is different from radiographic or ultrasonic techniques, where the reconstruction of defects is possible because the physical phenomena are governed by the wave equation. The time-reversal aspect of the wave equation permits the use of procedures such as holography and tomography to reconstruct defects. It is possible that defects can be reconstructed from EC data, but the reconstruction depends on the diffusion equation and one must rely on indirect algorithmic approaches to solve the inverse problem.[6] The "solution" to the inverse problem for EC techniques could be the use of pattern recognition algorithms to interpret the signals. The variations in shape of the trajectories of the signal in the impedance plane are used in pattern recognition schemes.

In addition to the ongoing work in this program, others have investigated the application of a three–dimensional (3–D) electromagnetic field analysis to predict EC response to defects.[7] Finite-element and boundary-element methods were applied to the EC problem. Experimental and calculated probe impedance trajectories for 100 and 400 kHz are presented for four 50% external slits with a width of 0.25 mm (0.010 in.), located 90° apart. The agreement between calculated and experimental (differential bobbin coil) data is satisfactory. Because the computer time required to perform 3-D calculations is very long, simplified 2-D analyses have been examined. Two– and 3-D analyses of EC signals at 100 and 400 kHz frequencies from 50 and 100% TW cracks in SG tubes were compared with experimental measurements. The results are qualitatively similar, but, quantitatively, the 3–D analysis appears significantly better (2–D

results were ≈1/2 of the experimental value). The problem with the 2–D analysis may be due to the lack of information about the volume of the crack.

Advances in digital signal processing may dramatically improve the ability to extract information from EC inspections. It may be possible to use sophisticated digital filters to solve problems that are now approached by multifrequency techniques, such as the elimination of signals from TSPs. Stepinski and Maszi[8] address the problem of detection and classification of material defects during an EC inspection. They consider algorithms for detecting and characterizing flaws and propose a new type of filter for classifying EC data. The new 2–D conjugate spectrum filters (CSFs) are sensitive to both phase angle and shape of the EC response. They transform all of the EC patterns into straight lines and thereby simplify the decision-making process. If digitized EC data that was sampled at a frequency synchronized with the inspection speed is available, CSFs could be used for SG tubing.

Rose et al.[3] describe a method for inspecting SG tubing with guided ultrasonic waves over long distances. The advantage of this concept is the absence of a moving probe and 100% coverage of the tube. Launching of guided waves with sufficient energy to inspect a long length of tubing is very difficult and sensitive to ultrasonic frequency, but theoretical considerations have significantly helped to optimize probe design. The ultrasonic wave is injected at the top of the tubing and travels the length of the tube with little attenuation. Echoes that return to the transmitting probe indicate defects in the tube. Defects that are only 10% of the total cross-sectional area have been detected in tubes nearly 17 m (55 ft) long. Tests have shown that guided waves can travel at least 49 m (160 ft). Although ultrasonic guided waves may be useful for inspection of SG tubing, satisfactory characterization of a detected flaw may not be possible for a fixed-probe configuration, because of the distortion of the ultrasonic wave as it propagates in the tube wall. The use of guided waves as part of a scanner, as described in this report, may be more effective for detecting circumferential cracks.

More recent developments were presented at the 17th EPRI Steam Generator NDE Workshop.[9] Some preliminary work on EC tomographic imaging was presented by French researchers, but the development is still in its infancy (Benoist et. al., CEA/CEREM and Savin, Framatome Technologies, Inc. [FTI]). The continuing effort requires development of sophisticated computer algorithms. Tomographic techniques are not expected to be used in real time or in-line but rather for more detailed off-line evaluation of flaws suggested by other EC procedures.

The results on EC array probes presented in Ref. 9 show that their reliability and sensitivity must be improved. The work to date suggests that arrays may be useful as an initial screening tool, but supplementary high-resolution rotating coil inspections will still be needed for verification. The difficulties associated with handling and analyzing data from multi-channel arrays may outweigh the potential improvements in detection capability over conventional bobbin inspections. Hardware requirements are more stringent, partly because special cables/wiring are needed and because the electronics are complex. It is also difficult to convert data from numerous coils (up to 32) into a conventional isometric image of the EC response, because of coil-to-coil variations in signal response and the difficulty in calibrating the array. Longer manual data analysis time offsets the time gained by faster scanning. If array probes are to replace bobbin coils as the initial screening tool, automated data analysis algorithms must be incorporated into the system.

A comparison of the performance of rotating (+Point™) and bobbin coil probes with that of array probes, including the Cecco-5, the MICA, and two Zetec arrays (a surface-riding array probe, and a nonsurface-riding probe) was presented (Raschiatore, Zetec). The MICA probe did not show significant improvement in reliability or detection over previous versions; in many cases, it exhibited the lowest sensitivity of the probes that were examined and was the least reliable during field tests. The sensitivity of the Cecco array probe to small defects was low.

Results were also presented at the workshop[9] on the Ghent rotating probe (Watts, Westinghouse NSD). The added complexity of this surface-riding transmit/receive rotating probe did not seem to lead to improved performance compared to the more widely used pancake and +Point™ probes. Although no comparative studies were presented, new and more complex rotating probes, such as P4-5 (i.e., Levy and Betsch, Intercontrolle), did not appear to show significant improvement over conventional rotating probes.

Five papers[9] addressed ultrasonic inspection of SG tubing. The number of presentations on UT methods at this meeting indicates a growing interest in the use of this technique to supplement or even replace EC testing. However, slow inspection speed, often significantly slower than that of rotating EC probes, and criticality of alignment still limit the use of UT as a supplementary NDE technique for SG tubing.

An evaluation of a 64-element annular ultrasonic phased array designed at Framatome was presented (Key, FTI and Quinn, Westinghouse). The array seems to perform better than mechanically rotated UT probes. Improvements in durability and redesign for compatibility with pusher–pullers are needed. A second paper on a phased ultrasonic array applied to inspection of the helical tube bundle of the French Super Phoenix reactor indicated that this system apparently worked well and allowed the inspection at the Super Phoenix reactor to be carried out at an acceptable inspection rate.

A paper on the depth sizing of circumferential SCC at the top of the tube sheet was presented (Krutzen, Nuson Inspection Services).[9] Four ultrasonic techniques were considered: echodynamic, time of flight diffraction, crack-tip echo, and guided wave. The crack tip echo technique was the most effective for sizing. However, no specific examples were presented. An increase in the use of ultrasonic techniques in ISIs is expected. Ultrasonic techniques can provide good estimates of the length and depth of cracks if a crack tip echo can be detected. However, the detection of a crack-tip echo from a SCC can be extremely difficult and unreliable, and obtaining depth estimates from crack tip echoes will require significant signal processing to improve S/N ratio.

References

1. D. R. Diercks, S. Bakhtiari, K. E. Kasza, D. S. Kupperman, S. Majumdar, J. Y. Park, and W. J. Shack, "Steam Generator Tube Integrity Program," Annual Report, Aug. 1995 - Sept. 1996, NUREG/CR-6511, ANL-97/3, Vol. 2, 1997.

2. C. V. Dodd, "Data Analysis for Steam Generator Tube Samples," Oak Ridge National Laboratory, NUREG/CR-6455, ORNL/TM-13206, 1996.

3. J. L. Rose, K. M. Rajana, and F. T. Carr, "Ultrasonic Guided Wave Inspection Concepts for Steam Generator Tubing," *Mater. Eval.*, pp. 307–311, Feb. 1994.

4. H. Houserman, R. Warlick, and R. Vollmer, "Using Satellite Technology to Improve SG Eddy Current Inspections," *Nucl. Eng. Int.*, Vol. 37(456), pp. 37–38, July 1992.

5. D. L. Atherton, D. D. Mackintosh, S. P. Sullivan, J. M. S. Dubois, and T. R. Schmidt, "Remote–Field Eddy Current Signal Representation," *Mater. Eval.*, pp. 782–789, July 1993.

6. S. J. Norton and J. R. Bowler, "Theory of Eddy Current Inversion," *J. Appl. Phys.*, Vol. 73(2), Jan. 15, 1993.

7. K. Satake, M. Tanaka, N. Shimizu, Y. Araki, and K. Morimoto, "Three–Dimensional Analysis on Eddy Current Testing for S/G Tubes," *IEEE Trans. Magn.*, Vol. 28(2), pp. 1466–1468, March 1992.

8. T. Stepinski and N. Maszi, "Conjugate Spectrum Filters for Eddy Current Signal Processing," *Mater. Eval.*, pp. 839–844, July 1993.

9. Proceedings of the 17th Annual EPRI Steam Generator NDE Workshop, EPRI Report TR-111547, Sept. 1998.

NRC FORM 335 (2–89) NRCM 1102, 3201, 3202

U. S. NUCLEAR REGULATORY COMMISSION

BIBLIOGRAPHIC DATA SHEET

(See instructions on the reverse)

1. REPORT NUMBER *(Assigned by NRC. Add Vol., Supp., Rev., and Addendum Numbers, if any.)*
NUREG/CR-6638
ANL-99/9

2. TITLE AND SUBTITLE
Advanced NDE for Steam Generator Tubing

3. DATE REPORT PUBLISHED
MONTH: January
YEAR: 2000

4. FIN OR GRANT NUMBER
W6487

5. AUTHOR(S)
S. Bakhtiari and D. S. Kupperman

6. TYPE OF REPORT
Technical; Topical

7. PERIOD COVERED *(Inclusive Dates)*

8. PERFORMING ORGANIZATION – NAME AND ADDRESS *(If NRC, provide Division, Office or Region, U.S. Nuclear Regulatory Commission, and mailing address; if contractor, provide name and mailing address.)*

Argonne National Laboratory
9700 South Cass Avenue
Argonne, IL 60439

9. SPONSORING ORGANIZATION – NAME AND ADDRESS *(If NRC, type "Same as above": if contractor, provide NRC Division, Office or Region, U.S. Nuclear Regulatory Commission, and mailing address.)*

Division of Engineering
Office of Nuclear Regulatory Research
U. S. Nuclear Regulatory Commission
Washington, DC 20555

10. SUPPLEMENTARY NOTES
J. Muscara, NRC Project Manager

11. ABSTRACT (200 words or less)

This report provides an assessment of various advanced nondestructive evaluation (NDE) techniques for inservice inspection of steam generator tubing. Selected results are presented on the application of data processing and visualization techniques; data analysis, including depth sizing and the development of correlations between eddy current signals and tube failure pressure by multivariate regression and neural networks; inspection of sleeved tubes; applications of ultrasonic NDE; and related work on emerging NDE technology.

12. KEY WORDS/DESCRIPTORS *(List words or phrases that will assist researchers in locating this report.)*
Steam Generator
Tubes
Stress Corrosion Cracking
Eddy Current Testing
Nondestructive Evaluation
In-service Inspection
Ultrasonic Inspection
Multivariate Analysis
Alloy 600

13. AVAILABILITY STATEMENT
Unlimited

14. SECURITY CLASSIFICATION
(This Page)
Unclassified
(This Report)
Unclassified

15. NUMBER OF PAGES

16. PRICE